
FEDERAL UNIVERSITY OF PARÁ

INSTITUTE OF TECHNOLOGY

POSTGRADUATE PROGRAM IN ELECTRICAL ENGINEERING

Cássio da Cruz Nogueira

# Design and Optimization of a 77 GHz Absorber for Autonomous Vehicles Using Artificial Neural Networks

Belém

2025

Cássio da Cruz Nogueira

# Design and Optimization of a 77 GHz Absorber for Autonomous Vehicles Using Artificial Neural Networks

Dissertation submitted to the Graduate Program in Electrical Engineering at the Institute of Technology as a partial requirement for obtaining the Master's Degree in Electrical Engineering.

Federal University of Pará

Supervisor: Prof° Dr. Miércio Cardoso de Alcântara Neto

Belém

2025

**Dados Internacionais de Catalogação na Publicação (CIP) de acordo com ISBD**
**Sistema de Bibliotecas da Universidade Federal do Pará**
**Gerada automaticamente pelo módulo Ficat, mediante os dados fornecidos pelo(a) autor(a)**

---

N778d Nogueira, Cássio da Cruz.
Design and Optimization of a 77 GHz Absorber for Autonomous Vehicles Using Artificial Neural Networks / Cássio da Cruz Nogueira. — 2025.
54 f. : il. color.

Orientador(a): Prof. Dr. Miércio Cardoso de Alcântara Neto

1. Absorbers. 2. Artificial Neural Networks (ANNs);. 3. Electromagnetic. 4. Equivalent Circuits. I. Título.

CDD 621.3

---

FEDERAL UNIVERSITY OF PARÁ
INSTITUTE OF TECHNOLOGY
GRADUATE PROGRAM IN ELECTRICAL ENGINEERING

# "DESIGN AND OPTIMIZATION OF A 77GHZ ABSORDER FOR AUTONOMOUS VEHICLES USING ARTIFICIAL NEURAL NETWORKS"

AUTHOR: **CÁSSIO DA CRUZ NOGUEIRA**

MASTER'S DISSERTATION SUBMITTED TO THE EXAMINING BOARD, APPROVED BY THE GRADUATE PROGRAM IN ELECTRICAL ENGINEERING, AND JUDGED ADEQUATE FOR THE OBTENTION OF THE DEGREE OF MASTER OF SCIENCE IN ELECTRICAL ENGINEERING IN THE AREA OF TELECOMMUNICATIONS.

APPROVED ON: 08/08/2025

**EXAMINING BOARD:**

gov.br Documento assinado digitalmente
MIERCIO CARDOSO DE ALCANTARA NETO
Data: 19/08/2025 10:10:00-0300
Verifique em https://validar.iti.gov.br

**Prof. Dr. Miércio Cardoso de Alcântara Neto**
(Advisor - PPGEE / UFPA)

gov.br Documento assinado digitalmente
FABRICIO JOSE BRITO BARROS
Data: 21/08/2025 11:24:34-0300
Verifique em https://validar.iti.gov.br

**Prof. Dr. Fabrício José Brito Barros**
(Internal Examiner - PPGEE / ITEC / UFPA)

gov.br Documento assinado digitalmente
BRUNO SOUZA LYRA CASTRO
Data: 19/08/2025 22:33:20-0300
Verifique em https://validar.iti.gov.br

**Prof. Dr. Bruno Souza Lyra Castro**
(External Examiner - CASTANHAL CAMPUS / UFPA)

gov.br Documento assinado digitalmente
NILTON RODOLFO NASCIMENTO MELO RODRIG
Data: 19/08/2025 12:25:00-0300
Verifique em https://validar.iti.gov.br

**Prof. Dr. Nilton Rodolfo Nascimento Melo Rodrigues**
(External Examiner - FEEB / UFPA)

**ENDORSEMENT**:

**Prof. Dr. Diego Lisboa Cardoso**
(Coordinator of PPGEE/ITEC/UFPA)

*I dedicate this work to my father David Nogueira and my beloved grandmother Anna Nogueira (In Memorian)...*

# Acknowledgements

The Computing and Telecommunications Laboratory (LCT) and the Technology Institute (ITEC) at the Federal University of Pará (UFPA) provided essential support and infrastructure for this study. The Graduate Program in Electrical Engineering (PPGEE) and the Office of Research and Graduate Studies (PROPESP) at UFPA also provided vital support. Financial support from the Coordination for the Improvement of Higher Education Personnel (CAPES) was crucial for the development of this work.

*"Nothing is impossible for those who persist "*
*(Alexander the Great)*

# Abstract

This work presents the design and optimization of a Frequency Selective Absorber (FSA) operating at 77 GHz, aimed at automotive radar and autonomous vehicle systems applications. The methodology combines computational modeling techniques, such as the Finite Element Method (FEM) and the Finite Integration Technique (FIT), with artificial neural networks (ANNs), specifically a multilayer perceptron (MLP), to optimize the geometric and material parameters of the absorber. The FSA structure comprises a Rogers Duroid RT5880 substrate and a copper metallic ground plane. The modeling employs an equivalent circuit with resonant elements (inductors, capacitors, and resistors) to describe the filter's behavior. We trained the ANN with simulation data, achieving high accuracy in predicting the optimal parameters, such as periodicity, substrate thickness, and aperture dimensions. Results demonstrate high absorber efficiency, with an absorption rate of 99.99% at the central resonance frequency of 77 GHz. The comparison between the ANN predictions and numerical methods (HFSS and CST Studio Suite) shows excellent agreement, validating the robustness of the proposed approach. The study concludes by highlighting the practical impact of the optimized design on enhancing the performance of automotive systems, emphasizing the potential of integrating ANNs into high-frequency electromagnetic device design.

**Keywords**: Absorbers; Artificial Neural Networks (ANNs); Electromagnetic; Equivalent Circuits.

# Resumo

Este trabalho apresenta o projeto e a otimização de um Absorvedor Seletivo de Frequência (ASF) operando a 77 GHz, direcionado a aplicações em sistemas de radar automotivo e veículos autônomos. A metodologia combina técnicas de modelagem computacional, como o Método dos Elementos Finitos (FEM) e a Técnica de Integração Finita (FIT), com redes neurais artificiais (RNAs), especificamente um perceptron multicamada (MLP), para otimizar os parâmetros geométricos e de material do absorvedor. A estrutura do Absorvedor é composta por um substrato Rogers Duroid RT5880 e um plano de terra metálico de cobre. A modelagem utiliza um circuito equivalente com elementos ressonantes (indutores, capacitores e resistores) para descrever o comportamento do filtro. A RNA foi treinada com dados de simulação, alcançando alta precisão na previsão dos parâmetros ideais, como periodicidade, espessura do substrato e dimensões das aberturas. Os resultados demonstram alta eficiência do absorvedor, com uma taxa de absorção de 99,99% na frequência central de ressonância de 77,5 GHz. A comparação entre as previsões da RNA e os métodos numéricos (HFSS e CST Studio Suite) mostrou excelente concordância, validando a robustez da abordagem proposta. O estudo conclui destacando o impacto prático do projeto otimizado na melhoria do desempenho de sistemas automotivos, enfatizando o potencial da integração de RNAs no projeto de dispositivos eletromagnéticos de alta frequência.

**Palavras-chave**: Absorvedores; Redes Neurais Artificiais (RNAs); Eletromagnetismo; Circuitos Equivalentes.

# Resumen

Este trabajo presenta el diseño y la optimización de un Absorbedor Selectivo en Frecuencia (ASF) que opera a 77 GHz, dirigido a aplicaciones de radar automotriz y sistemas de vehículos autónomos. La metodología combina técnicas de modelado computacional, como el Método de Elementos Finitos (FEM) y la Técnica de Integración Finita (FIT), con redes neuronales artificiales (RNAs), específicamente un perceptrón multicapa (MLP), para optimizar los parámetros geométricos y materiales del absorbente. La estructura del ASF está compuesta por un sustrato Rogers Duroid RT5880 y un plano de tierra metálico de cobre. El modelado utiliza un circuito equivalente con elementos resonantes (inductores, capacitores y resistores) para describir el comportamiento del filtro. Entrenamos la RNA con datos de simulación, logrando una alta precisión en la predicción de los parámetros óptimos, como la periodicidad, el grosor del sustrato y las dimensiones de las aperturas. Los resultados demuestran una alta eficiencia del absorbente, con una tasa de absorción del 99.99% a la frecuencia de resonancia central de 77.5 GHz. La comparación entre las predicciones de la RNA y los métodos numéricos (HFSS y CST Studio Suite) muestra una excelente concordancia, validando la robustez del enfoque propuesto. El estudio concluye destacando el impacto práctico del diseño optimizado en la mejora del rendimiento de los sistemas automotrices, enfatizando el potencial de integrar las RNAs en el diseño de dispositivos electromagnéticos de alta frecuencia.

**Palabras clave**: Absorbedores; Redes Neuronales Artificiales (RNAs); Electromagnético; Circuitos Equivalentes.

# List of illustrations

# List of tables

# List of abbreviations and acronyms

| | |
|---|---|
| SRR | *Short Range Radar* |
| ITU | International Telecommunication Union |
| ADAS | *Advanced Driver Assistance Systems* |
| FSS | *Frequency Selective Surface* |
| AFSS | *Active Frequency Selective Surface* |
| RFSS | *Reconfigurable Frequency Selective Surface* |
| ANN | Artificial Neural Network |
| UFPA | Federal University of Pará |
| mm | Millimeters |
| LCT | Laboratory of Computing and Telecommunications |
| GHz | Gigahertz |
| EM | Electromagnetic Structures |
| FEM | *Finite Element Method* |
| FIT | *Finite Integration Technique* |
| HFSS | *High-Frequency Structure Simulator* |
| MEMS | *Micro-Electro-Mechanical Systems* |

# List of symbols

| | |
|---|---|
| $Dx$ | Periodicity |
| $met$ | Copper layer thickness |
| $esps$ | Thickness of the Roger Duroid 5880 substrate |
| $l$ | Height of the diamond-shaped structure |
| $w$ | Width of the diamond-shaped structure |
| $pt$ | Ground plane thickness |
| $\varepsilon_r$ | Relative dielectric constant |
| $\delta$ | *Skin Depth* (penetration depth) |
| $\sigma$ | Electrical conductivity of the conductor |
| $\mu_r$ | Relative permeability of the material |
| $\mu_0$ | Magnetic permeability of free space |
| Hz | Hertz (unit of frequency) |
| $f_r$ | Resonant frequency |
| $c$ | Speed of light in a vacuum |
| $\lambda$ | Wavelength |
| $\epsilon$ | Electric permittivity |
| $\mu$ | Magnetic permeability |
| $A$ | Absorption efficiency |
| $T$ | Transmission coefficient |

# Contents

# 1 Introduction

The growing demand for advanced automotive systems, driven by emerging technologies such as autonomous vehicles, has accelerated the development of increasingly efficient automotive radars [1, 2]. These systems enhance road safety by reducing the frequency and severity of accidents. Radars play a critical role in precise object detection, contributing to safety and reliability in both urban and highway environments. In particular, Advanced Driver Assistance Systems (ADAS) utilize radars for functionalities such as imminent collision detection, lane change assistant, blind spot monitoring, and autonomous parking [3, 4].

For these applications, the 77 GHz frequency has proven ideal due to its high resolution and capability to operate under adverse weather conditions [2, 5]. Additionally, the International Telecommunication Union (ITU), in its ITU-R M.2057-1 report, recommends that vehicular radars operate within the 76–81 GHz range [6], establishing the 77 GHz as the standard for long-range detection in automotive systems [7].

The efficiency of these radars can be compromised by electromagnetic interference and unwanted reflections, which affect detection accuracy, however, to mitigate these effects, electromagnetic absorbers play a key role in eliminating reflected signals and optimizing radar performance. Within this context, selective absorber filters (SAFs) stand out due to their ability to selectively absorb specific frequencies, offering superior efficiency and design flexibility for high-frequency applications [8–13].

To address the challenge of unwanted signal interference, this study explores the use of absorbers to eliminate such signals. Metasurfaces, known for their remarkable electromagnetic wave absorption properties, offer a promising solution. These materials are characterized by their thin profiles and design flexibility across a wide frequency range, from microwave to optical [9, 10]. This innovation represents a significant improvement over existing commercial absorbers for 77 GHz applications [14, 15].

Advances in computational methods have significantly impacted industrial and engineering research [16]. Computational techniques are increasingly employed for simulating and acquiring parameters of complex systems. However, the growing demand for precision and the increasing complexity of devices result in time-consuming simulation processes, where evaluating a single criterion can take hours, days, or even weeks [17]- [18]. Thus, developing methods to reduce simulation time and improve optimization is crucial for saving time and financial resources [19].

In this study, we present the development of a selective absorber filter (SAF) operating at 77 GHz, employing a hybrid approach that combines numerical techniques

and artificial intelligence. The absorber design was modeled using Ansys HFSS (based on the Finite Element Method, FEM) and CST Studio Suite (employing the Finite Integration Technique, FIT). Both methods are widely used for analyzing and optimizing high-frequency electromagnetic devices, ensuring accurate parameter simulations for the absorber.

In addition to numerical simulations, this study employs artificial neural networks (ANNs) as an optimization tool. The ANNs, specifically the multilayer perceptron (MLP) model, were trained with simulation-generated data, enabling precise predictions of geometric and material parameters that maximize absorption efficiency. Complementarily, an equivalent circuit model, comprising inductors, capacitors, and resistors, was developed to validate the obtained results and provide a robust theoretical analysis of the SAF's resonant behavior.

The results demonstrate an absorption efficiency exceeding 99.99% at the 77.5 GHz resonance frequency, validating the effectiveness of the proposed methodology. This work not only advances the design of electromagnetic absorbers but also paves the way for innovative solutions in automotive radar and wireless communication systems, where precision and reliability are critical factors.

# 2 Frequency Selective Surfaces - FSS

Frequency Selective Surfaces (FSS) are passive or not, two-dimensional structures composed of metallic elements arranged on a dielectric substrate, forming an infinite array and applied in spatial filters [17, 20, 21]. In active (Active Frequency Selective Surface - AFSS) or reconfigurable (Reconfigurable Frequency Selective Surface - RFSS) arrays, the coupled voltage generators must have the same amplitude and linear phase variations along the array [22]. In Figure 1, the two-dimensional shape of a periodic band-reject structure is shown [17]. In Figure 2, an example of an AFSS suggested by [23] is shown.

Figure 1. Two-dimensional geometry of a periodic band-reject structure. (a) Arrangement, (b) Periodicity.

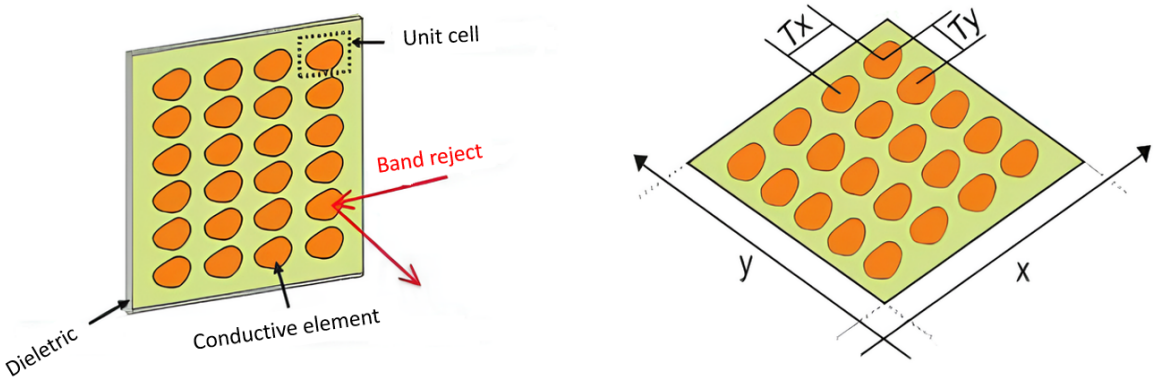


Source: Adapted from [17].

Figure 2. Simulation of an AFSS structure in the HFSS model.

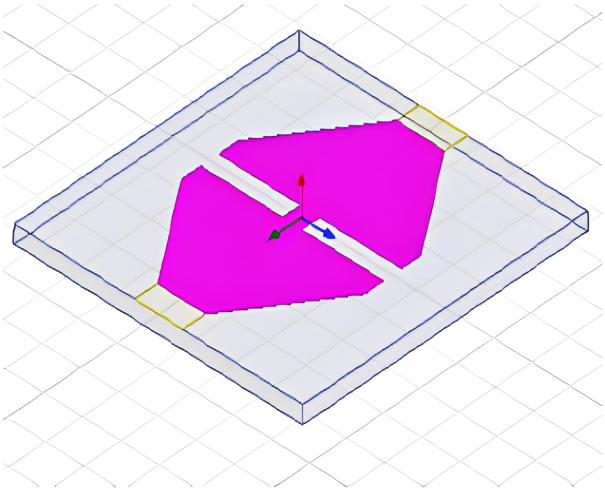

Source: Adapted from [23].

The earliest scientific studies on frequency selective surfaces trace their roots to the analysis of diffraction gratings in optics, a physical principle initially investigated by David Rittenhouse and Francis Hopkinson in 1786 [24]. Diffraction gratings were used to decompose non-monochromatic light beams into their spectral components [20].

Literature reports indicate that David Rittenhouse, an experienced physicist, investigated optical diffraction gratings based on an observation made by Francis Hopkinson, who noticed a phenomenon when viewing a lamp through a silk handkerchief [25]. In the experiment, Rittenhouse observed that some bands of the light spectrum were suppressed when white light was filtered [25]. This phenomenon demonstrated that it is possible to decompose a monochromatic light beam into specific bands of the spectrum, depending on the analyzed frequencies and the physical characteristics of the apertures [26], [20], [24].

Advances in the field of FSS were accelerated by the creation of printed circuit boards by Paul Eisler (1936), which provided easier-to-build, low-volume, and low-cost equipment, ranging from basic radios to satellites [25].

Due to their great potential in military applications, studies on FSS intensified in the 1960s. Subsequently, they expanded to applications in devices and services for communication systems in the terahertz, millimeter, and submillimeter wave bands [25].

Depending on the geometry of the metallizations in its unit cell, an FSS can function as a bandpass filter, with slot-type elements, or a band-reject filter, with patch-type elements [27]. Figure 3 shows, respectively, a slot-type FSS and a patch-type FSS [28].

Figure 3. Types of FSS and their frequency responses. a) Slot type b) Patch type.

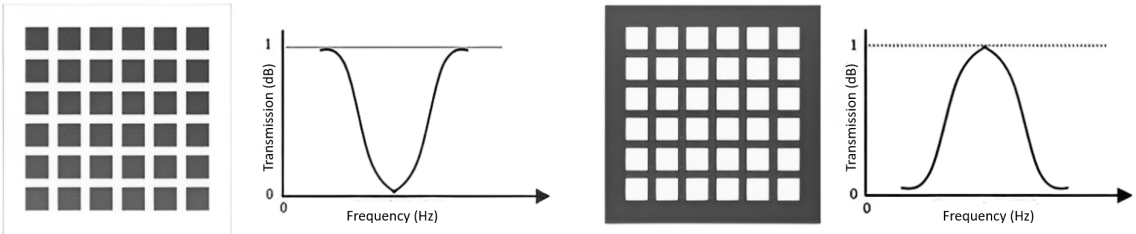


Source: Adapted from [28].

The application of this device is determined during the design phase according to the specific requirements to be met. This will determine its filtering behavior in specific frequency bands, comparable to electronic frequency filters used in RF. For instance, a planar slot-type FSS can be developed to allow the passage of low frequencies and reflect high frequencies according to a specific pattern [27]. The metallizations of the unit cell resonate, reflecting the wavelength corresponding to the frequency. This functions as a bandpass filter as shown in Figure 3(a). A patch-type FSS functions as a band-reject

filter, but when the elements resonate, the structure reflects the incident wave within the wavelength range corresponding to the desired frequency band, resulting in total wave reflection, as shown in Figure 3(b).

## 2.1 Common Geometrical Shapes for FSS

Frequency Selective Surfaces (FSS) can be classified in various ways, based on the geometry of their elements. The shape of the unit cell is one of the main factors affecting the frequency response of FSS [26]. This characteristic makes geometry one of the most adjustable aspects in the design of FSS. According to [29], [26], and [30], the geometric elements can be categorized into four main groups:

In this section, the elements used are grouped into four distinct categories, as proposed by [26]. Group 1 consists of N-pole elements connected at the center. Group 2 comprises loop-type elements, while Group 3 includes solid internal elements. Finally, Group 4 is composed of combinations of two or three elements from the previous groups. Figures 4 to 7 present examples of each of these groups.

Figure 4. Group 1 - Center-fed N-pole Elements. (a) Thin Dipole, (b) Crossed Dipole, (c) Tripole, (d) Jerusalem Cross.

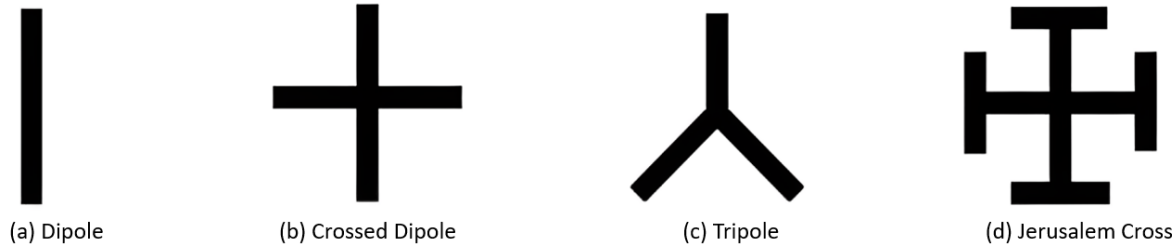


Source: Adapted from [26].

Figure 5. Group 2 - Loop Elements. (a) Square Loop, (b) Double Square Loop, (c) Square Loop with Grid, (d) Concentric Circular Rings.

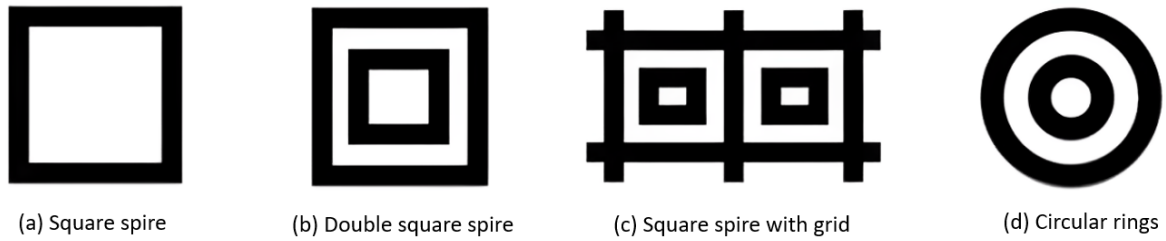


Source: Adapted from [26].

Figure 6. Group 3 - Solid Internal Elements. (a) Square Patches, (b) Rectangular Patches, (c) Hexagonal Patches, (d) Circular Patches.

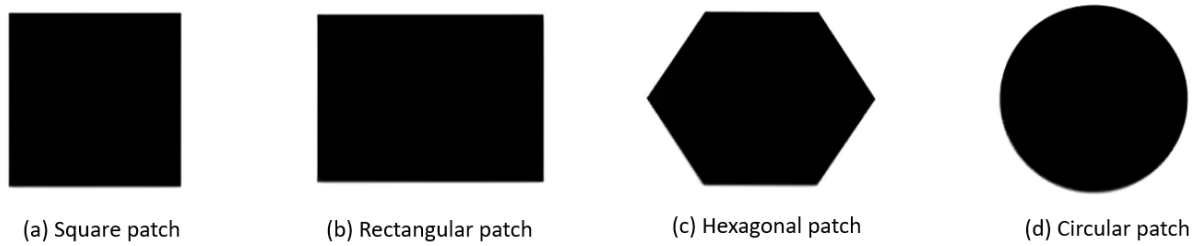


Source: Adapted from [26].

Figure 7. Group 4 - Combinations of Elements from Groups 1, 2, and 3.

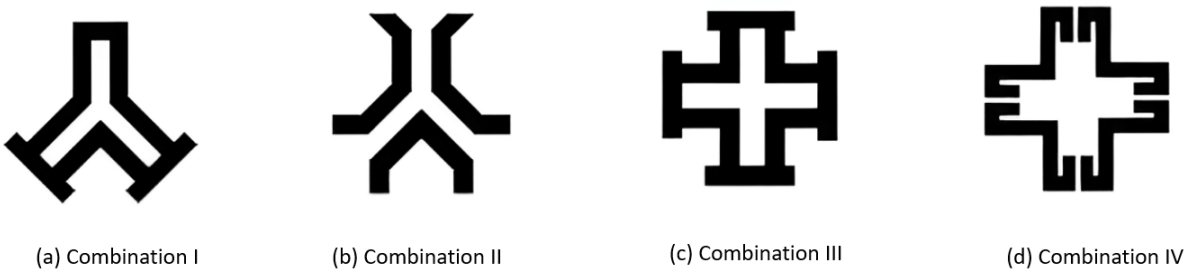


Source: Adapted from [26].

## 2.2 Classification of FSS Based on Metallization Layer Thickness

Frequency Selective Surfaces (FSS) can be categorized based on the thickness of their metallization layer, resulting in two main types: thin sheets and thick sheets. The choice between these categories significantly influences the performance and applicability of FSS in various contexts [31].

### 2.2.1 Thin sheet

Thin sheet Frequency Selective Surfaces (FSS) are characterized by a metallization layer with a thickness less than $0,001\lambda_0$, where $\lambda_0$ represents the wavelength corresponding to the FSS resonance frequency in free space. These structures are often fabricated using printed circuit board technology, offering advantages such as reduced weight, smaller size, and lower costs. The miniaturization enabled by this configuration makes thin sheet FSS an attractive option for applications requiring compact and cost-effective solutions [29], [30]. Figure 8 presents an example of a thin sheet FSS, as demonstrated by [31].

Figure 8. Representation of a thin bulkhead FSS.

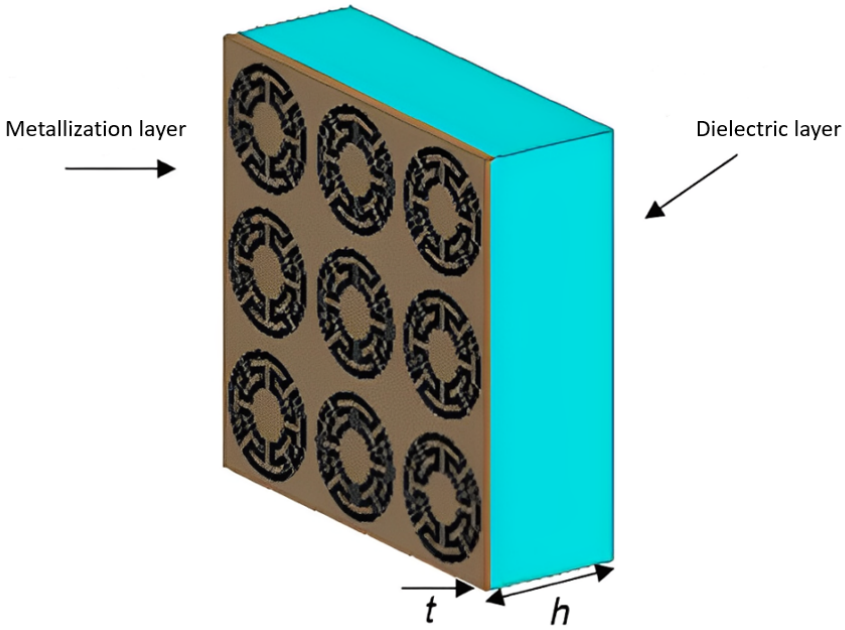


Source: Adapted from [31].

### 2.2.2 Thick sheet

Thick sheet Frequency Selective Surfaces (FSS) are characterized by a thicker metallization layer or even two metallization layers separated by a dielectric material. This structure is illustrated in Figure 9, as demonstrated by [31]. Thick sheet FSS offer advantages such as a steeper transition from the passband to the stopband and a flatter passband. However, they also present disadvantages, such as increased weight, fabrication complexity, and higher costs [32], [33], [34].

Figure 9. Representation of a double-layer thick-sheet FSS with a dielectric spacer.

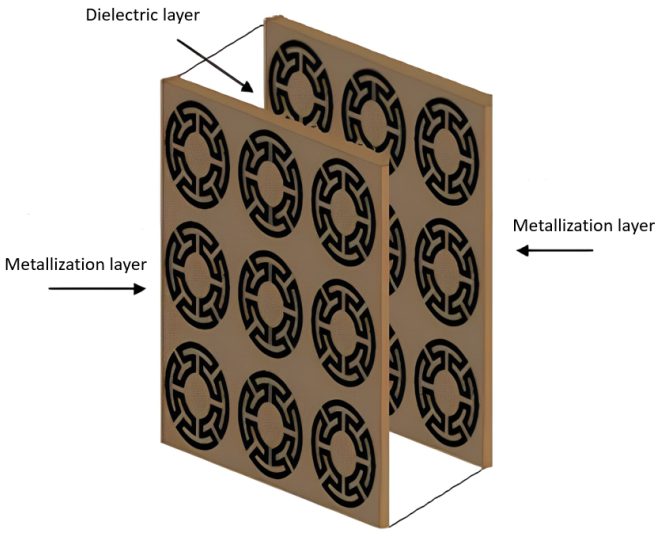


Source: Adapted from [31].

### 2.2.3 Reconfiguration of arrays

Frequency Selective Surfaces (FSS) can also be classified based on their reconfigurability [31]. They are divided into two main categories: passive FSS and reconfigurable FSS (RFSS), as illustrated in Figure 10, as demonstrated by [35]. Passive FSS have a fixed frequency response, which simplifies the design and fabrication process [36].

Figure 10. FSSReconfigurable FSS with dual-polarized annular geometry

Source: Adapted from [35].

On the other hand, reconfigurable FSS incorporate active devices such as diodes,

varactors, and MEMS switches, which can be biased to modify their electromagnetic properties [28–30, 32–34, 37]. Another approach to reconfiguration involves mechanical adjustments to the FSS array arrangement [35, 36, 38, 39].

### 2.2.4 Some FSS Applications

Due to their frequency filtering characteristics in specific bands, these two-dimensional (or three-dimensional) planar periodic structures used at high frequencies have inspired researchers in the field of applied electromagnetism (EM). These structures can also be used as wideband or multiband structures [28].

Their applications include antenna reflectors, radomes, electromagnetic shields, angular filters, and microwave absorbers, as well as military applications and wireless network security [21], [29], [38].

In Figure 11, the FSS is used as a sub-reflector in an antenna capable of operating in two distinct bands. This structure is placed between two feed elements that radiate at different frequencies and the main reflector. The surface is designed to reflect the frequency band associated with the resonance $F_{R1}$, with a bandwidth $B_{W1}$ corresponding to **Feeder 1**. Simultaneously, the surface is almost totally transparent to the operating band of 'Feeder 2', with frequencies $F_{R2}$ and $B_{W2}$. This configuration allows for frequency reuse, enabling two feed elements, each operating at a distinct frequency, to share the same reflector antenna simultaneously [39].

Figure 11. FSS-based reflector antenna representation.

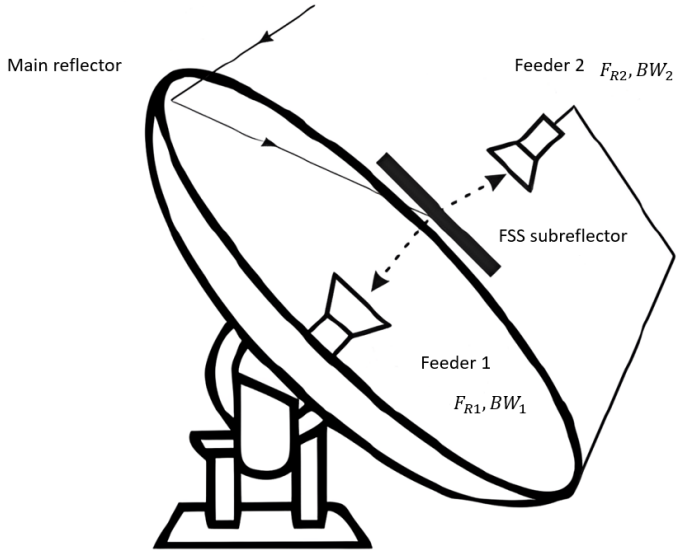


Source: Adapted from [39].

The door panel of a household microwave oven, as illustrated in Figure 12, is a notable example of FSS application [40]. The oven operates by generating electromagnetic

waves in the range of approximately 2.45 GHz, which can be harmful to human health [39]. In this context, the FSS is designed to significantly attenuate these waves, acting as a filter that allows the passage of the visible light frequency range [26, 29, 30, 41].

Figure 12. Frequency selective surface for microwave oven doors.

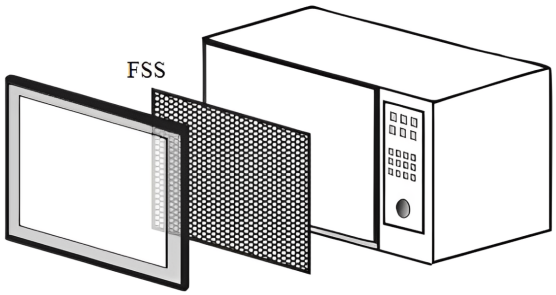


Source: Adapted from [40].

Radomes are structures designed to protect and support the antenna and its feed elements [37]. The FSS is used within the antenna's operating band, acting as a bandpass filter [42]. Structurally, the FSS can be embedded between two dielectric layers that compose the radome. This configuration helps to minimize radiation outside the antenna's operating band, reducing unwanted interference [43–45]. Figure 13 illustrates a practical application of FSS in radomes, as presented by [46].

Figure 13. Application of FSS in radomes.


Source: Adapted from [46].

Smart walls also utilize FSS, relying on the principle of interference propagation as demonstrated in Figure 14 found in the work of [47]. These structures reduce the risk of unauthorized access to information by preventing unwanted transmissions or receptions. Additionally, they can function as wallpaper, protecting the data flow of local wireless networks [39]. The FSS acts as a filter with specific rejection bands for the frequency range used in the propagation of wireless network signals, such as Wi-Fi and WLAN [48], [47].

Figure 14. Performance of smart walls in indoor environments.

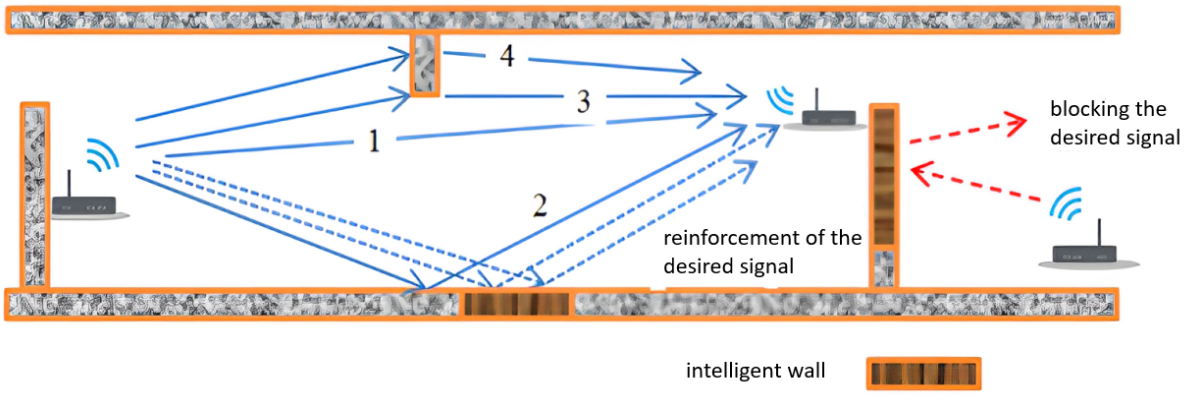


Source: Adapted from [47].

## 2.3 Absorbers

Absorbers operate by converting the energy of the incident electromagnetic wave into heat, dissipating part of the field intensity that reaches the material. In their fundamental form, these structures are designed to absorb wave signals in a specific band or multiple frequency bands, depending on their design. In this way, they play a crucial role in minimizing the reflection and transmission of unwanted waves, improving the efficiency and performance of communication systems and electronic devices [25].

Conceptually, absorbers are devices designed to act as spatial filters that neither transmit nor reflect electromagnetic signals in a specific frequency range [25]. The efficiency of an absorber depends on its characteristics of minimum thickness and maximum bandwidth, as well as the ability to reduce the reflection of signals in the desired frequency range [49].

Figure 15. Illustration of a cross-slot absorber: (a) layer structure and (b) unit cell dimensions.

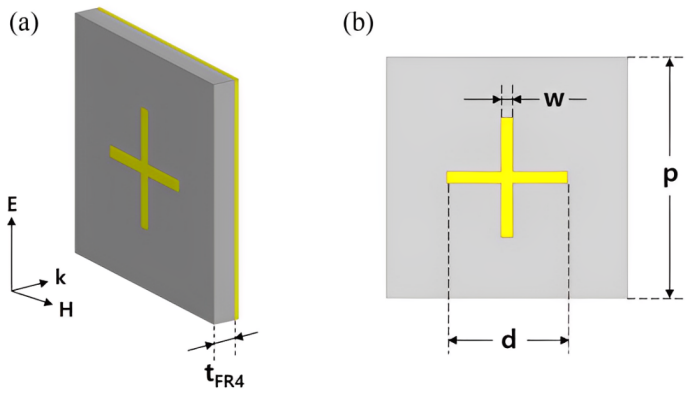


Source: Adapted from [25].

The type of absorber to be used in a project is primarily determined by the intensity of the signal to be absorbed or attenuated, the desired frequency band, and the structural aspects of the application. The main factors limiting the design of the structure and, consequently, affecting the results and applications, include the dielectric material, the thickness and weight of the structures, which influence the absorption bandwidth and the level of reflectivity in the operating band [49–51].

The level of reflectivity of the structure determines the efficiency of the absorber and is governed by the difference between the impedance of free space and the impedance of the absorbing structure, with the insertion of electromagnetic waves being performed normally or obliquely on its surface. This level of reflectivity is a direct consequence of the respective geometries and materials used in the design of the structure, including electrical permittivity and magnetic permeability characteristics [50, 52].

### 2.3.1 Absorber FSS

Frequency Selective Absorbers (FSAs) are advanced structures that represent a modification of conventional absorbers. In these absorbers, the complete metal sheet or ground plane is replaced by a frequency selective surface (FSS), and the resistive layer is also organized in periodic arrays [25].

FSS structures generally exhibit high reflectivity characteristics in the desired band. When associated with absorber configurations, these structures can significantly reduce reflection values in some frequency bands, approaching zero and thus characterizing wave signal absorption [25]. Figure 16 illustrates the performance of a conventional FSS structure and the same structure with absorber characteristics [53]. It can be observed that, with the combination of the configurations, electromagnetic (EM) waves are absorbed instead of reflected, and absorption occurs in different frequency bands, maintaining the transmission band [53].

Figure 16. (a) FSS configuration e (b) Absorbing FSS.

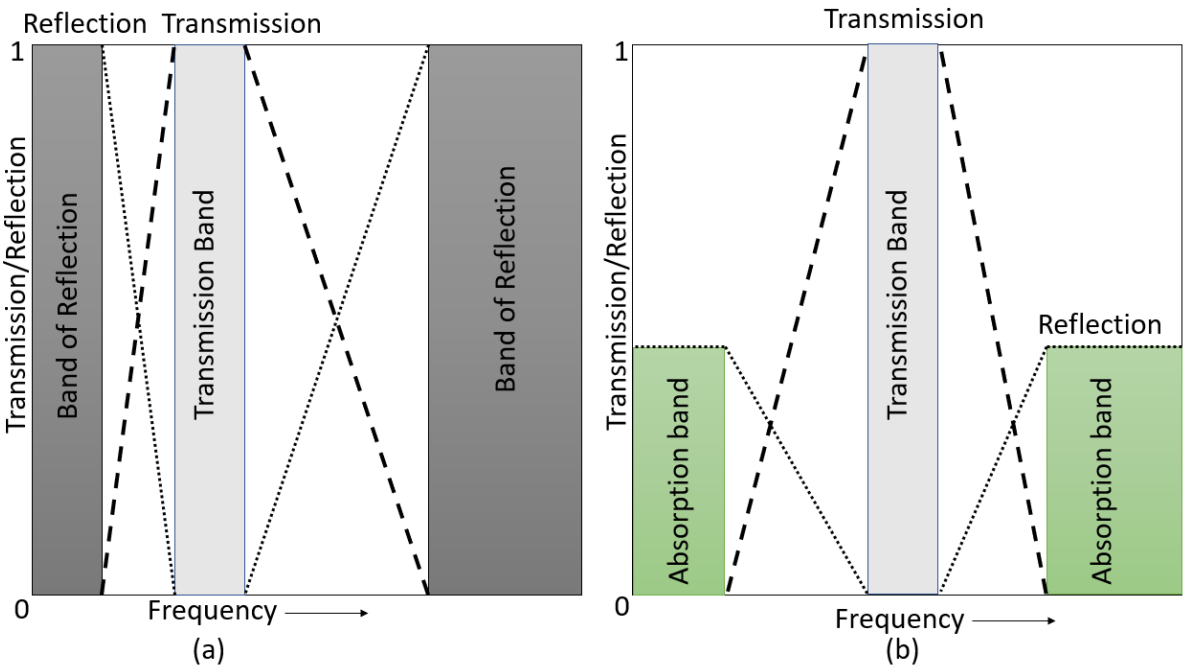


Source: Adapted from [53].

# 3 Modeling and Numerical Simulation

The simulations were conducted on a machine equipped with a 12th-generation Intel(R) Core(TM) i5-12400 processor operating at an average frequency of 2.50 GHz and 16.00 GB of RAM. The operating system used was 64-bit Windows 11. After completing the simulations and compiling the database, the results were provided to the Artificial Neural Network (ANN) for training, aiming to capture the absorber's behavior concerning parameter variations.

To model the electromagnetic behavior of the Selective Absorber Filter (SAF) at 77 GHz, the Ansys HFSS and CST Studio Suite software were employed, utilizing the Finite Element Method (FEM) and the Finite Integration Technique (FIT), respectively. These methods are widely recognized for their accuracy in simulating high-frequency devices, particularly in absorber configurations.

The CST Studio Suite employs the Finite Integration Technique (FIT), a numerical method for solving differential equations that represent electric and magnetic fields in materials and structures within the fields of electrical engineering and computer science [54].

This technique involves discretizing the problem domain into a finite mesh and numerically solving the differential equations. It facilitates the analysis of complex and anisotropic materials. The precision and efficiency of the FIT depend on the quality of the mesh and numerical integration techniques, which may require significant computational resources, particularly for three-dimensional or high-frequency problems [55].

Ansys HFSS calculates the electric field ($E$) using the Finite Element Method (FEM). The solution domain is divided into physically conformal tetrahedral finite elements, and the electric field $E$ within each element is approximated using local basis functions [56]. These approximation functions are derived from the differential form of Maxwell's equations.

Maxwell's equations are transformed into matrix equations when fields are represented in this manner. The resulting matrix equation is sparse, as each element is directly related only to its neighbors, and is solved using an efficient sparse matrix solver. Since the electric field is being computed, the solution domain must include the region where the electric fields exist [56].

## 3.1 Structure Modeling

The structure of the selective absorber filter (SAF) was developed using the Rogers Duroid RT5880 substrate, known for its low loss and high stability properties at elevated frequencies [57]. This substrate has a relative dielectric constant of 2.2, a thickness of 1.27

mm, and a loss tangent of 0.0009, which are crucial properties for ensuring the optimized performance of the absorber. The metallic layers are made of copper, with a thickness of 0.035 mm on both the ground plane and the top conductive layer.

The geometric configuration of the SAF incorporates a central diamond-shaped slot, carefully designed to maximize absorption at 77 GHz. This innovative geometry promotes effective resonance, enabling robust and selective absorption of incident electromagnetic waves. Figure 17 shows the unit cell of the SAF structure, highlighting the diamond-shaped slot.

Figure 17. Unit cell of the absorber.

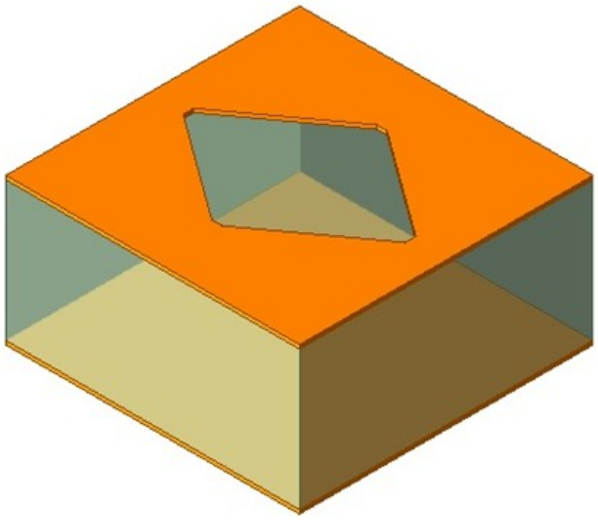

Source: Elaborated by the author.

Figure 18 displays the periodic arrangement of the unit cells, illustrating the complete planar absorber layout. This figure is essential for understanding the detailed structure and geometric arrangement of the filter.

Figure 18. Periodic arrangement of unit cells.

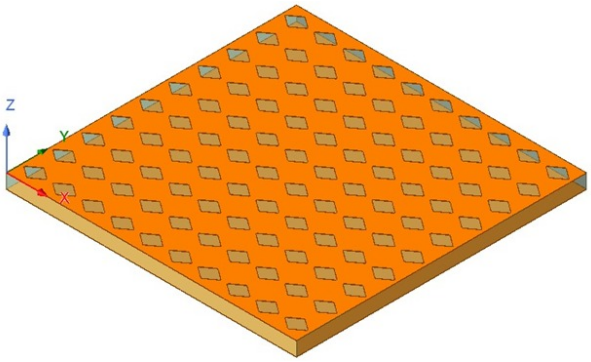


Source: Elaborated by the author.

The length and width of the diamond-shaped slot are represented by $l$ and $w$,

respectively, while the absorber's periodicity is denoted as $D_x = D_y$ as illustrated in Figure 19(a). The thicknesses of the substrate, copper layer, and ground plane are represented by esps, met, and ground, as illustrated in Figure 19(b).

Figure 19. Unit cell dimensions. (a) Geometry of the diamond-shaped slot, with length $l$, width $w$, and absorber's periodicity $D_x = D_y$. (b) Front view showing the thicknesses of the substrate (esps), copper layer (met), and ground plane (ground).

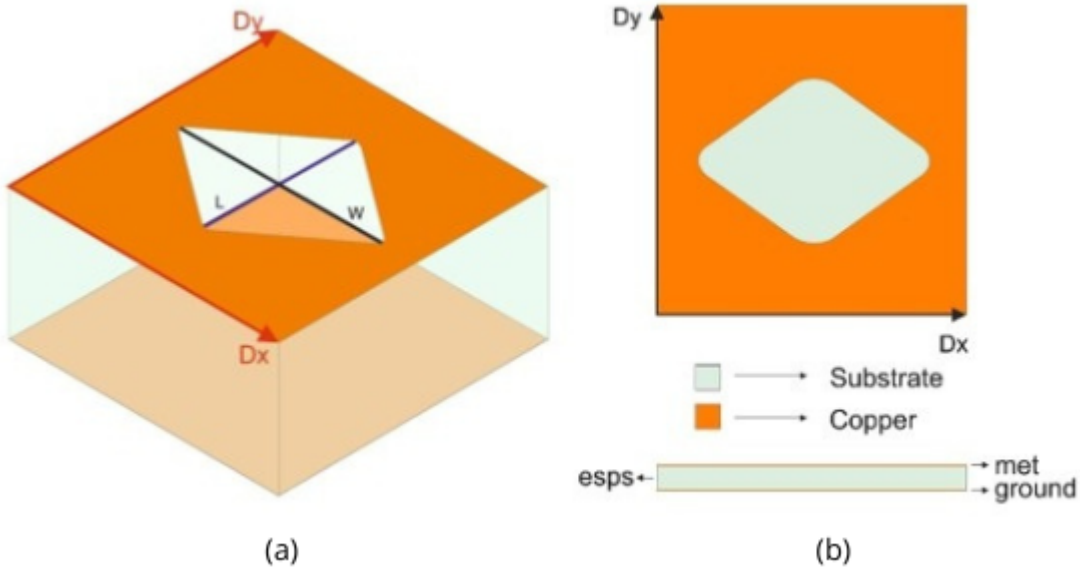


Source: Elaborated by the author.

In Equation 3.1, $f_r$ represents the absorber's resonant frequency, a fundamental parameter for the unit cell's frequency response. This equation relates the structure's geometric dimensions to its resonant frequency, serving as an initial tool in the design process. Based on it, adjustments were made to refine the cell dimensions, ensuring the resonant frequency aligns with the target operational frequency. This step is essential to optimize the filter's performance, guaranteeing its effectiveness in the 77 GHz.

$$f_r = \frac{c}{\lambda\sqrt{\varepsilon_r}} = \frac{c}{(w-l)\sqrt{\varepsilon_r}} \tag{3.1}$$

The variables in Equation 3.1 are defined as follows: $c$ is the speed of light in a vacuum, $\lambda$ is the wavelength of the electromagnetic wave in question, $\varepsilon_r$ is the relative dielectric constant of the absorber's material, and $w$ and $l$ are the absorber structure's specific dimensions (width and length, respectively).

The numerical simulations were configured with ideal boundary conditions to replicate plane wave excitation over a frequency range of 75 to 80 GHz. Periodic boundary conditions were applied to the excitation of electromagnetic waves, ensuring continuity

and uniformity of the incident field. This setup allowed simulation of the SAF's response to multiple incidence directions, focusing on an analysis of perpendicular polarization relative to the absorber's surface.

Each simulation conducted in HFSS and CST Studio Suite considered a parametric variation of the SAF dimensions, including the width and height of the central slot and the structure's periodicity. The results of each variation were used to observe the device's resonant behavior and identify the geometric configuration providing the highest absorption rate at 77 GHz.

The reflection and transmission coefficients were analyzed using Equations 3.2 and 3.3, which describe the relationship between the $S_{11}$ and $S_{21}$ parameters with the reflectance (R) and absorptance (A) of the structure. This approach enabled the calculation of the fraction of energy reflected and absorbed, providing a quantitative analysis of the SAF's performance.

$$R = |S_{11}|^2 \tag{3.2}$$

$$A = 1 - R - T = 1 - |S_{11}|^2 - |S_{21}|^2 \tag{3.3}$$

Based on this data, an Artificial Neural Network (ANN) was subsequently trained to predict and optimize the material's geometric parameters, accelerating the fine-tuning process of the design.

This numerical modeling and simulation approach provides a robust foundation for experimental validation and the development of highly efficient absorbers in the 77 GHz, with direct application to automotive radar systems.

The simulation was conducted parametrically, with one variable altered per simulation while the others remained constant. This method generated a comprehensive dataset of absorptance and reflectance values, which were saved for future analysis. CST Microwave Studio was used to perform 366 simulations, all within the 75–80 GHz range. Each simulation examined a specific variable, such as the diamond-shaped slot angle, periodicity, width ($w$), height ($l$), and metal thickness. For example, while adjusting the slot angle in 1-degree increments, all other parameters were held constant.

The simulations used the following baseline dimensions: a 10° slot angle, periodicity ($Dx$) of 2.88 mm, metamaterial substrate thickness of 1.27 mm, diamond slot width ($w$) of 1.85 mm, diamond slot height ($l$) of 1.84 mm, and copper thickness of 0.35 mm. After each simulation, the absorptance and reflectance results were processed using MATLAB code to generate graphs populating the dataset. This dataset was then used to train a multilayer perceptron (MLP) neural network aimed at optimizing the absorber's performance.

To theoretically validate the results obtained in the simulations, an equivalent circuit model was developed using the resonant circuit technique [26, 58] in conjunction with the HFSS Circuit Design tool. This model, consisting of two inductors, two capacitors, and two resistors, was designed to replicate the resonant behavior of the FSA. Initially, the inductances and capacitances were calculated based on theoretical equations related to the dimensions of the absorber and the permittivity of the substrate, while the resistors modeled the losses due to absorption. These equations were employed as a starting point, considering the need for an initial approach due to the context of millimeter waves. Subsequently, the values of the circuit components were adjusted iteratively to achieve a better match between the resonant frequency obtained from the theoretical model and the numerical simulations.

The equivalent circuit was designed based on the resonant response of the FSA, taking into account the properties of the substrate and the conductive layers. The equivalent structure consists of two inductors (L1 and L2), two capacitors (C1 and C2), and two resistors (R1 and R2), as illustrated in Figure 20.

Figure 20. FSA Equivalent Circuit Diagram.

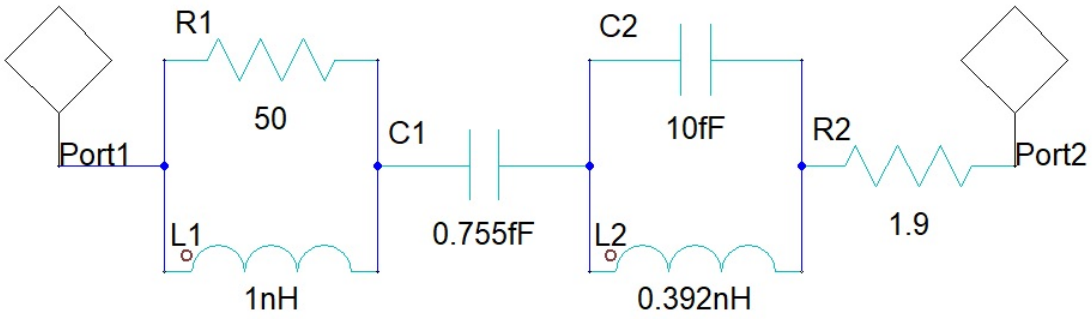


Source: Elaborated by the author.

The selection and values of these components are based on the dimensions of the FSA aperture and the dielectric properties of the Rogers Duroid RT5880 substrate. The inductors and capacitors represent the energy storage capability and phase response of the structure, while the resistors model the losses due to electromagnetic absorption.

To calculate the inductance ($L$) and capacitance ($C$) of the equivalent structure, the geometry of the frequency selective surface (FSA) and the interaction of the electromagnetic field along the aperture edge were considered. The inductance for the aperture structure was estimated using Equation 3.4, considering the permeability of free space ($\mu_0$), the

relative permeability of the material ($\mu_r$), the effective width ($W_{\text{eq}}$), and the effective length of the aperture ($L_{\text{eq}}$).

$$L \approx \frac{\mu_0 \cdot \mu_r \cdot L_{\text{eq}}}{2 \cdot \pi} \cdot \ln\left(\frac{2 \cdot L_{\text{eq}}}{W_{\text{eq}}}\right) \tag{3.4}$$

The capacitance was calculated based on the effective area of the aperture ($A_{\text{eff}}$) and the permittivity of the substrate ($\epsilon_0$ and $\epsilon_r$), as shown in Equation (3.5).

$$C \approx \frac{\epsilon_0 \cdot \epsilon_r \cdot A_{\text{eff}}}{d} \tag{3.5}$$

For resonance and operating frequency, the following equation applies:

$$f_o \approx \frac{1}{2\pi\sqrt{L \cdot C}} \tag{3.6}$$

The equivalent circuit model showed excellent agreement with the simulation results obtained from HFSS and CST Studio Suite. Figure 21 presents the comparison between the frequency response of the equivalent circuit and the simulation results, showing close correspondence in both the resonant frequency and the absorption characteristics.

Figure 21. Comparison between the Frequency Response of the Equivalent Circuit and the HFSS and CST Simulations.

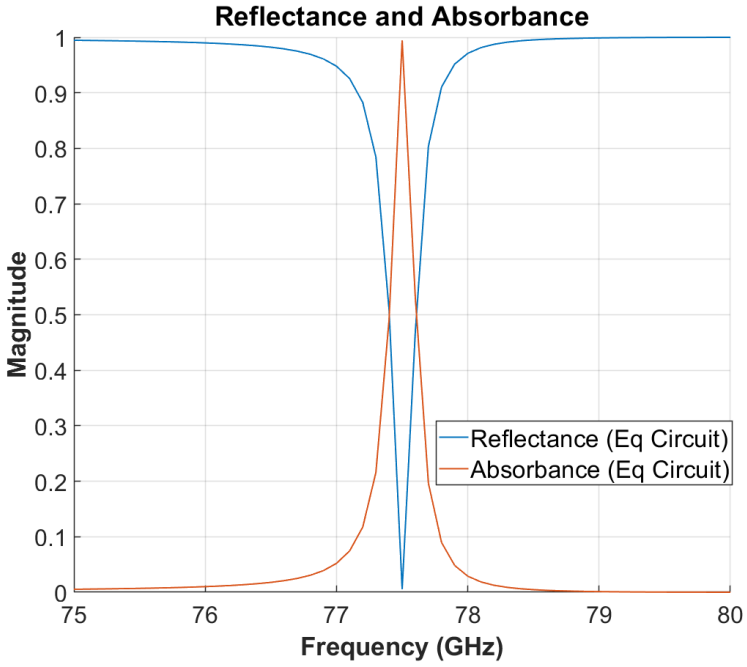


Source: Elaborated by the author.

This model provides a solid theoretical foundation for the analysis of the resonant behavior of the FSA and validates the proposed methodology for optimizing electromagnetic absorbers.

## 3.2 Artificial Neural Network

The neural network was trained with simulation data obtained from numerical models performed with the CST Studio Suite software. These data include variations in geometric parameters, such as the width and height of the opening, the periodicity of the structure, and the substrate thickness, resulting in a dataset with 366 simulations, all within the range of 75 GHz to 80 GHz. The network's input consisted of the diamond opening angle, reflectance, absorbance, and resonance frequency, while the output consisted of geometric variables.

As illustrated in Figure 22, a Multi-Layer Perceptron (MLP) neural network was used, consisting of a hidden layer with 7 neurons. The network has 4 neurons in the input layer, corresponding to the input variables: frequency, absorbance, reflectance, and incidence angle. In the output layer, the network also has 4 neurons, which generate the main FSA dimensions: $Dx$, $l$, $w$, and $esps$. The MLP structure was designed to correlate the input parameters with the FSA dimensions, providing high accuracy in predicting geometric values.

The activation function used was the log-sigmoid, commonly employed in regression problems such as this study. The training was carried out using the Levenberg-Marquardt algorithm, which is efficient in terms of fast convergence and accuracy.

Figure 22. Diagram of the neural network.

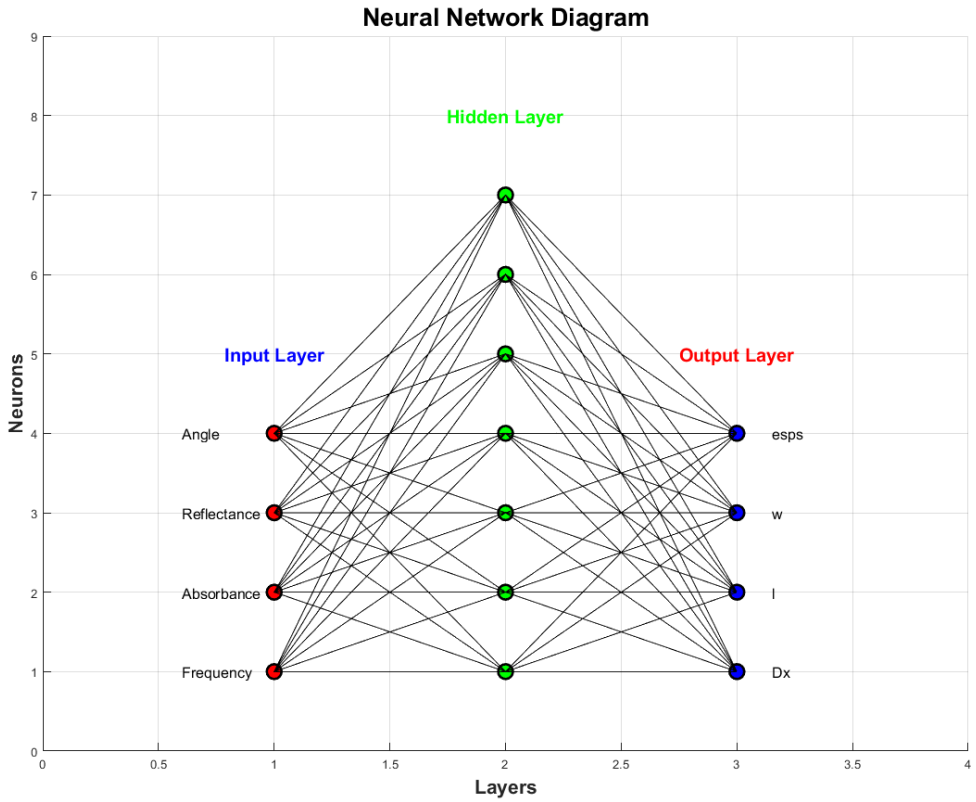


Source: Elaborated by the author.

To ensure the model's effectiveness, the dataset was divided into two parts: 70% for training and 30% for testing. Due to the small sample size, no separate validation set was reserved. During training, the neural network weights were adjusted using the training set, while the test set was used to evaluate the model's performance and its ability to generalize.

Validation was performed directly on the test set to minimize the risk of overfitting. After each training epoch, the error on the test set was calculated, allowing continuous adjustments and validation of the model's accuracy. Figure 23 shows the performance of the neural network throughout the process, with direct monitoring of the test set.

The network structure was optimized through various configurations, in order to balance complexity and performance [59, 60]. It is important to note that the lack of a separate validation set may limit the assessment of the model's performance. Therefore, best practices such as cross-validation or establishing a separate validation set could be implemented in future analyses to improve the robustness of the results.

Figure 23. Performance of the neural network in different design configurations.

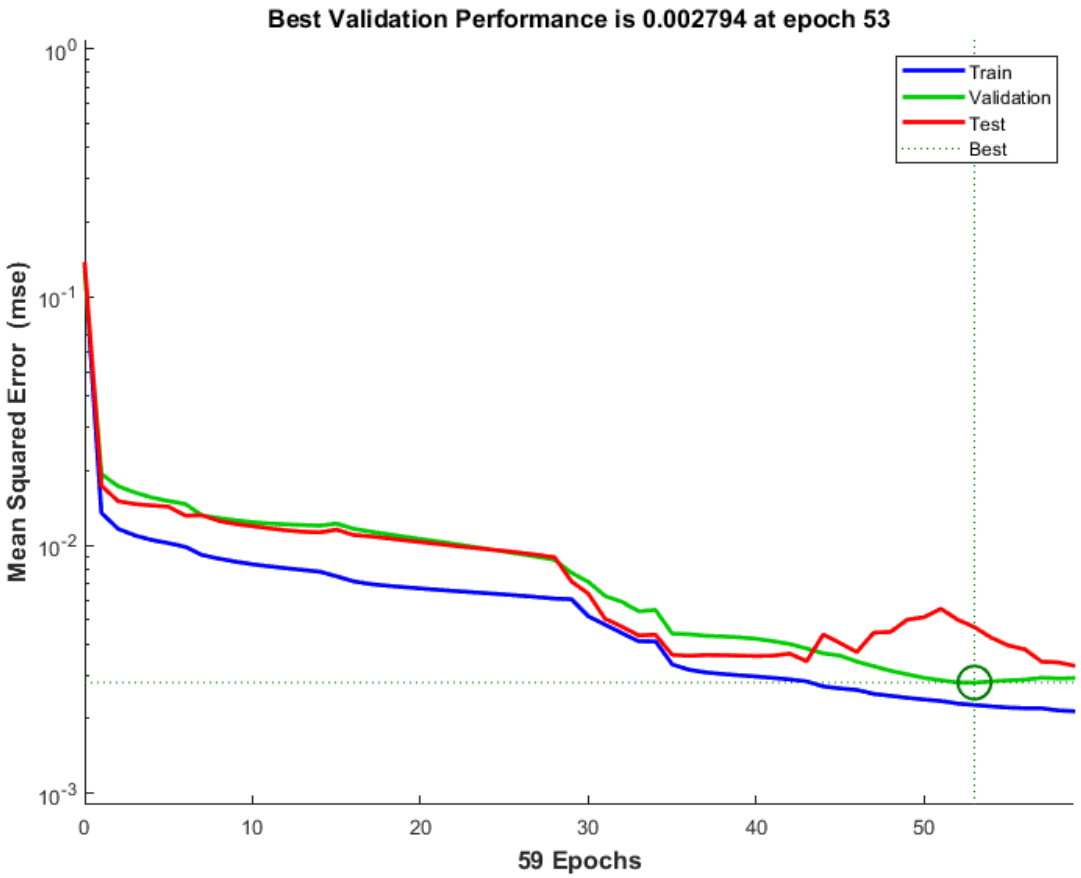


Source: Elaborated by the author.

Figure 24 illustrates the neural network's performance across various evaluation stages. In Figure 24(a), the correlation graph during the training phase highlights the ANN's ability to fit the observed data accurately. Figure 24(b) focuses on the validation phase, showcasing the model's capacity to generalize to unseen data. Figure 24(c) evaluates the testing phase, depicting the ANN's performance on entirely independent datasets. Finally, Figure 24(d) provides the overall correlation graph, consolidating all phases and offering a comprehensive view of the network's accuracy across the entire dataset.

Figure 24. Performance of the neural network across different stages. (a) Correlation graph during the training phase. (b) Correlation graph during the validation phase. (c) Correlation graph during the testing phase. (d) Overall correlation graph combining all phases.

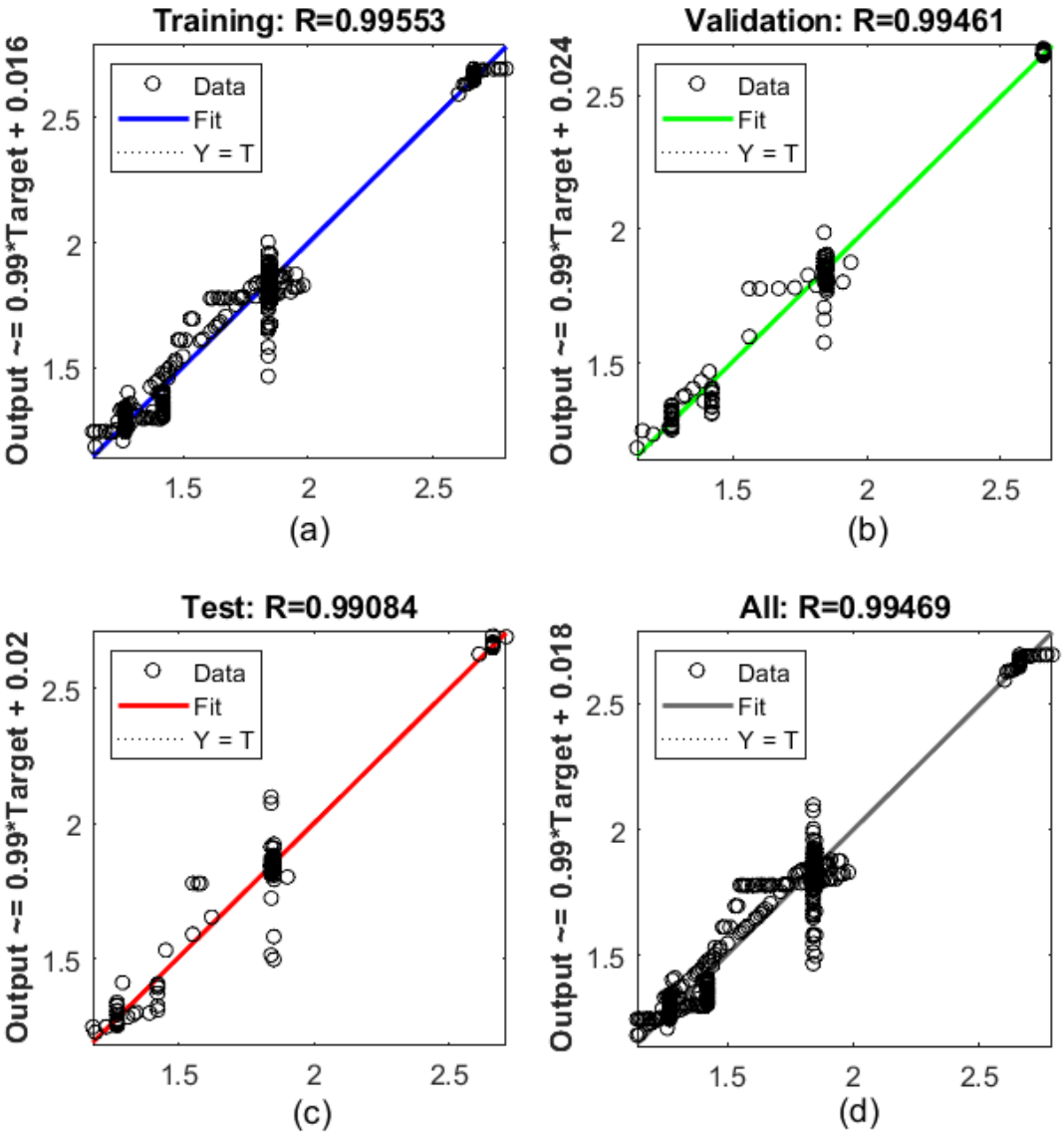


Source: Elaborated by the author.

The evolution of the stopping criteria during the neural network training is presented in Figure 25. Figure 25(a) illustrates the gradient's behavior, which stabilizes at low values, indicating convergence. Figure 25(b) shows the adjustment of the update parameter $\mu$ to smaller values, reflecting the algorithm's adaptation to minimize the error. Lastly, Figure 25(c) depicts the increase in validation failures, which ultimately reach the limit of 6, triggering the training halt to prevent overfitting and enhance the model's generalization capabilities.

Figure 25. Monitoring of stopping criteria during neural network training. (a) Evolution of the gradient, showing stabilization. (b) Update parameter $\mu$, which decreases during training. (c) Validation failures, progressively increasing to the defined limit.

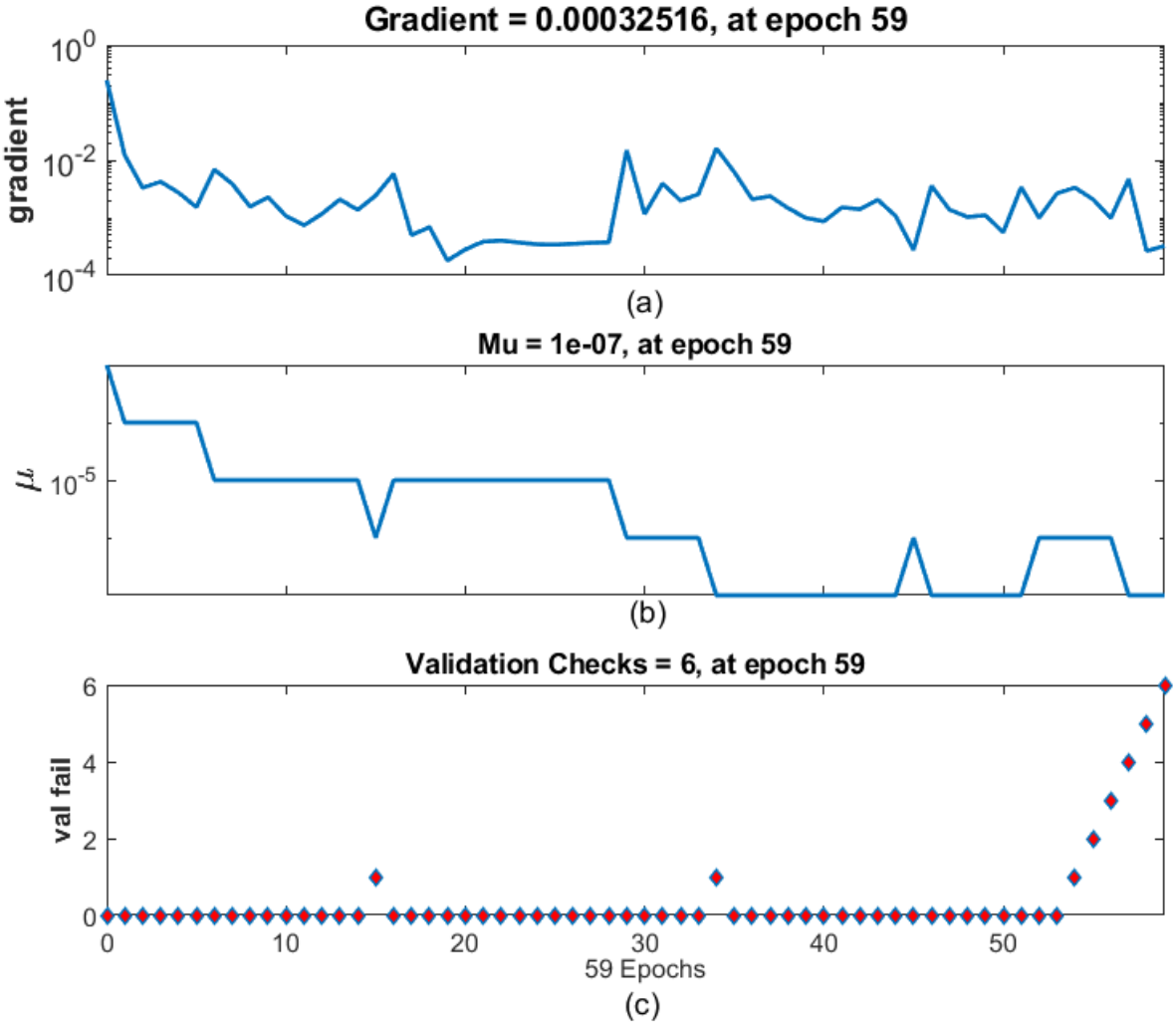


Source: Elaborated by the author.

After training, the ANN was able to predict the ideal parameters with high accuracy, especially the substrate dimensions, which achieved R-squared coefficients of up to 0.99469, indicating excellent performance in predicting these parameters. Table 1 presents the optimized parameter values that were applied in the simulations performed with HFSS (Finite Element Method) and CST Studio Suite (Finite Integration Technique). The table 1 below shows the optimized parameters by the ANN:

The results obtained show an excellent match between the values predicted by the ANN and those simulated by CST, as illustrated in Figure 26. Figure 26(a) presents the parameter $Dx$, demonstrating high prediction accuracy with minimal deviations from the simulated results. Figure 26(b) shows the parameter $W$, where the predictions closely align

Table 1. Optimized Parameter Values

| Parameter | Value | Description |
|---|---|---|
| **Periodicity (Dx)** | 2.6765 | Distance between the centers of the openings |
| **Substrate thickness (esps)** | 1.2618 | Thickness of ROGERS RT5880 substrate |
| **Height of the diamond (l)** | 1.3060 | Absorber opening height |
| **Width of the diamond (w)** | 1.8301 | Absorber opening width |

with the simulations. Similarly, Figure 26(c) illustrates the parameter $L$, also reflecting high accuracy. For the *Esps* parameter, shown in Figure 26(d), the discrepancies are slightly larger yet remain within acceptable limits, showcasing the robustness of the ANN even under varying conditions. These results emphasize the ANN's effectiveness in modeling the absorber filter's geometric behavior.

Figure 26. Comparison between simulated and ANN-predicted results for geometric parameters. (a) *Dx*: Absorber periodicity. (b) $W$: Slot width. (c) $L$: Slot length. (d) *Esps*: Substrate thickness.

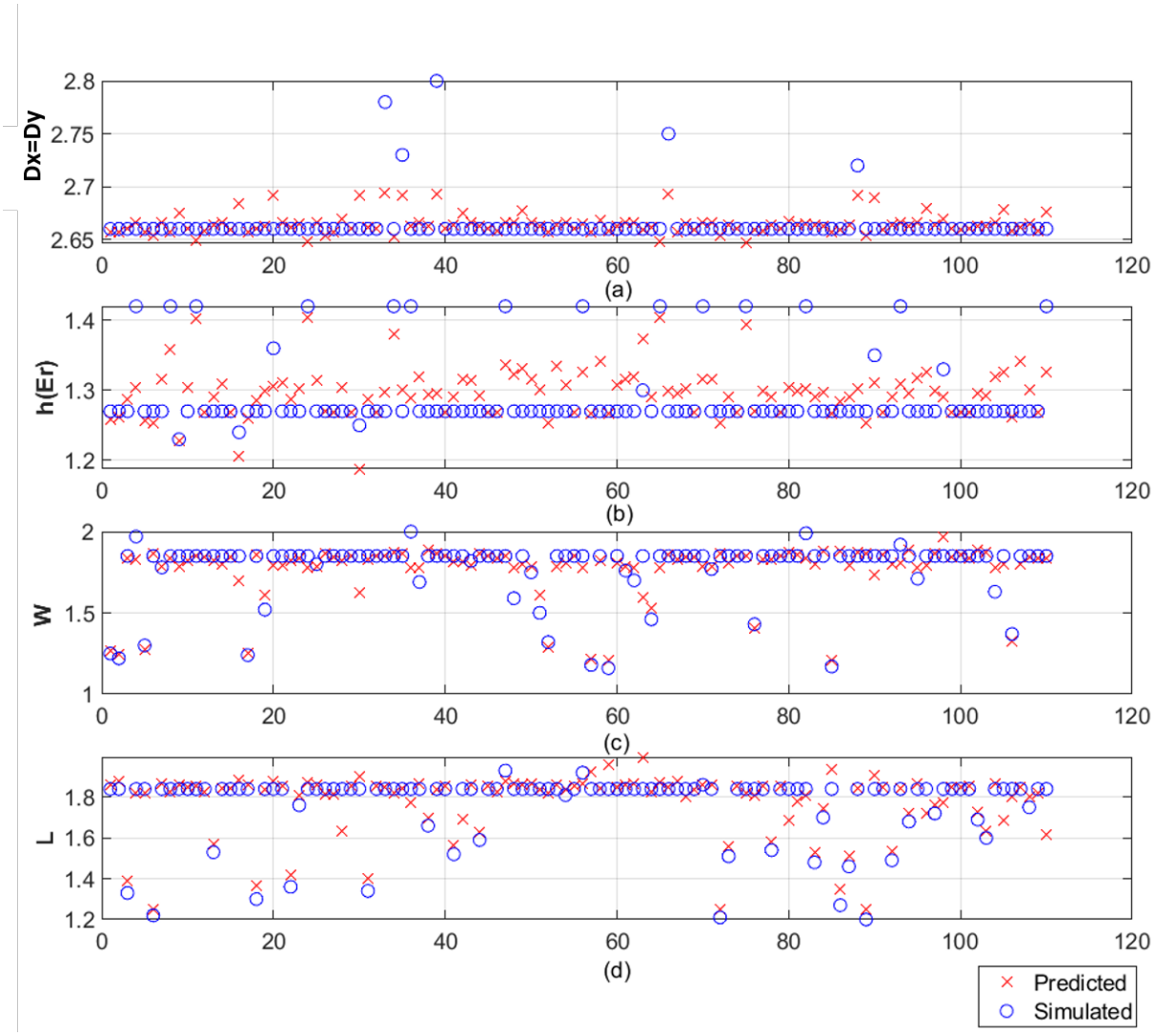


Source: Elaborated by the author.

These results confirm the potential of the ANN as a tool for optimization in millimeter-wave frequency designs, significantly reducing development time by minimizing reliance on extensive simulations. The performance achieved reinforces the feasibility of integrating artificial intelligence techniques into advanced design processes, especially for applications at 77 GHz frequencies.

# 4 Results

## 4.1 Effect of Slot Angle Variation

Figure 27 shows the simulated absorption and reflectance results as a function of frequency when the slot opening angle is varied between 10°, 40°, and 70°. To isolate the effect of the slot angle, all other parameters, including $D_x$, $esps$, $met$, $w$, and $l$, were kept constant during these simulations, which were performed using CST Studio Suite. It was observed that an increase in the slot angle led to a decrease in absorption and also shifted the resonant frequency. This effect occurs due to the modification in the distribution of electromagnetic fields, which alters the impedance coupling, directly impacting the absorber's absorption efficiency [61].

Figure 27. Simulated results of absorption and reflectance as a function of frequency with variation of slot angles, using CST Studio Suite.

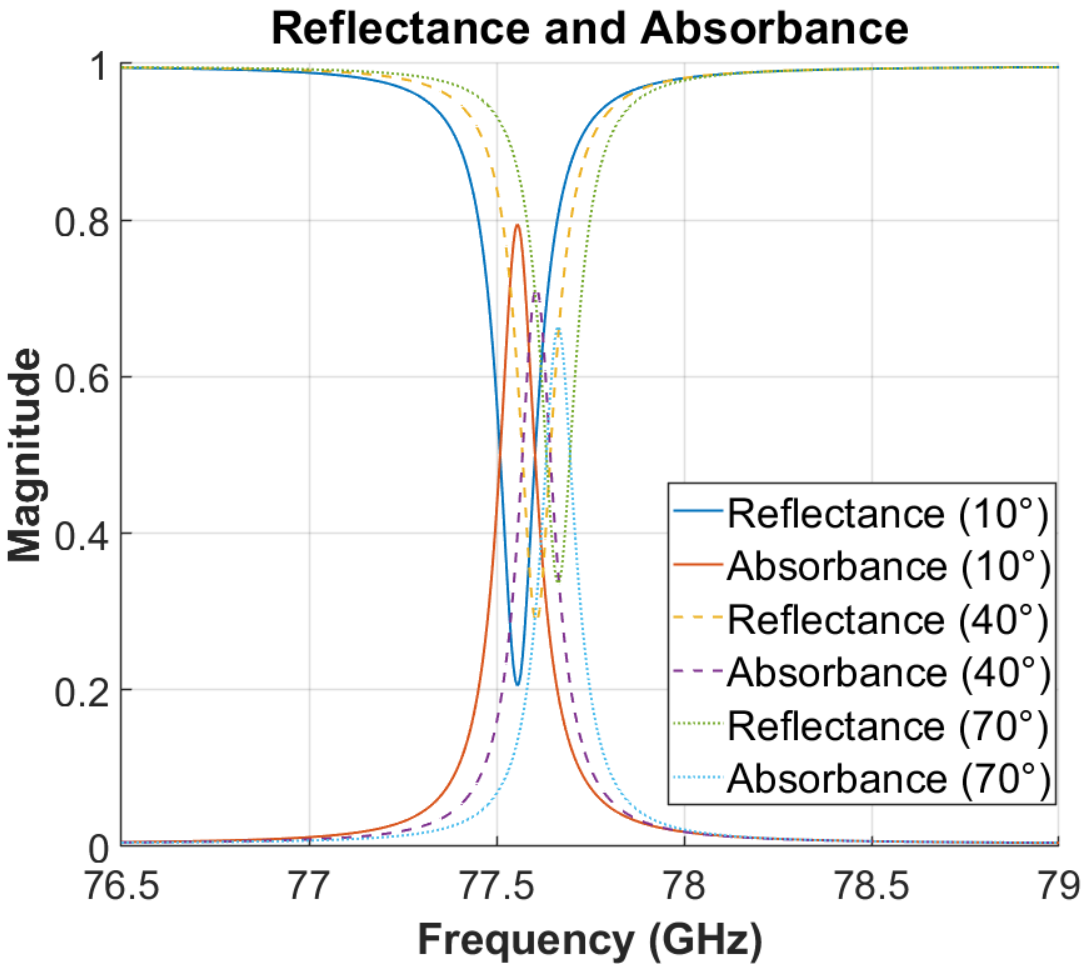


Source: Elaborated by the author.

## 4.2 Effect of Periodicity

Figure 28 illustrates the impact of the unit cell periodicity variation on the resonant frequency. The simulations were performed for values of $D_x = 2.66$ mm, 2.71 mm, and 2.76 mm, with the slot angle fixed at 10° and the substrate thickness of 1.27 mm. The variation in periodicity resulted in a shift in the resonant frequency, highlighting the importance of this parameter in the absorber's performance.

Figure 28. Simulated results in CST with periodicity variation.

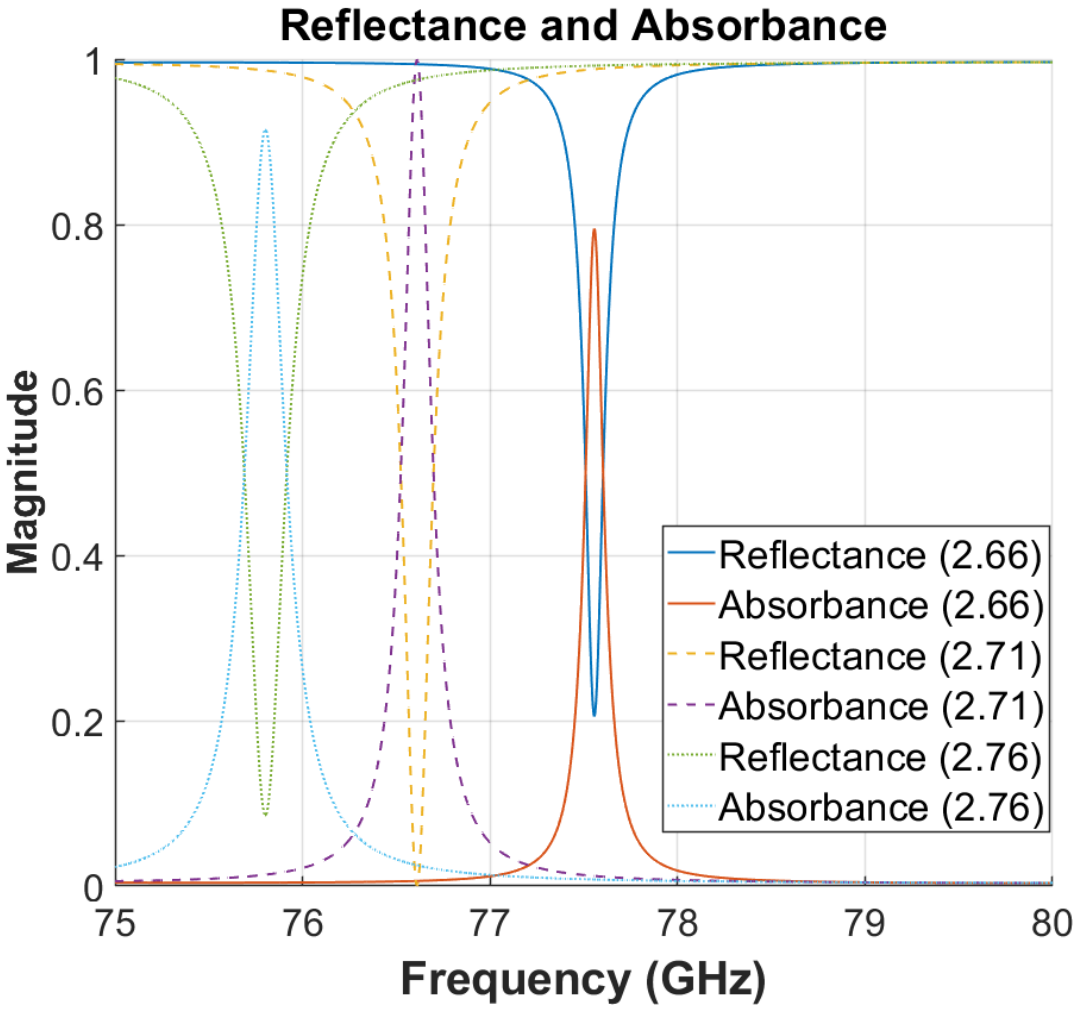


Source: Elaborated by the author.

## 4.3 Effect of Diamond Length and Width

Figure 29 shows the impact of the diamond's length and width on absorption efficiency. The diamond angle was kept at 10°, and the width $w$ was fixed at 1.85 mm, while the length $l$ varied between 1.80 mm, 1.60 mm, and 1.40 mm. The analysis of the results showed that the variation in the diamond length directly affected the absorption

capacity of the device.

Figure 29. Results obtained with the variation of diamond length, using CST Studio Suite.

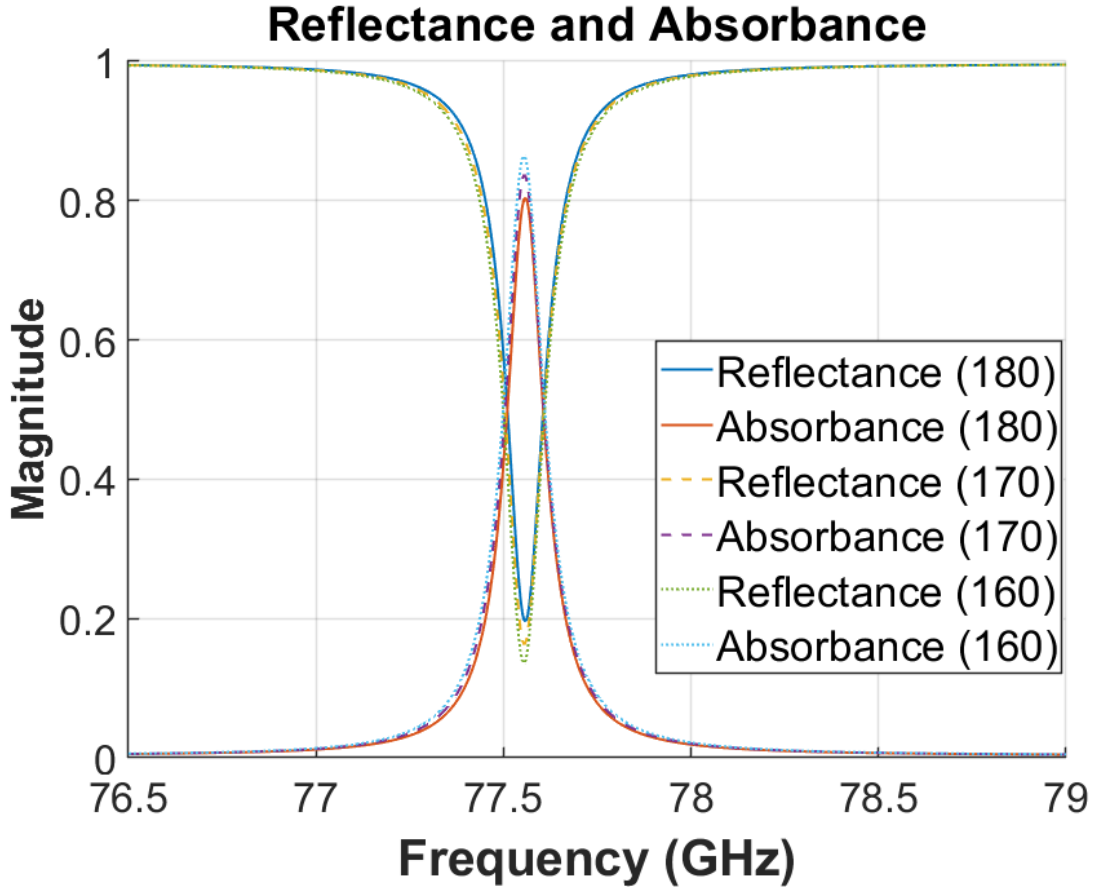


Source: Elaborated by the author.

## 4.4 Results Obtained with the Artificial Neural Network (ANN) Associated with the Equivalent Circuit

The parameters optimized by the ANN ensured an accurate and efficient response, resulting in an absorber with a resonant frequency of 77.5 GHz and an absorption rate of 99.99%, as shown in Figure 30. The comparison between the ANN results and the HFSS and CST simulations confirms the accuracy of the optimization.

Figure 30. Results obtained using the ANN, comparing the HFSS and CST results. Identical values confirm the validation of both numerical methods.

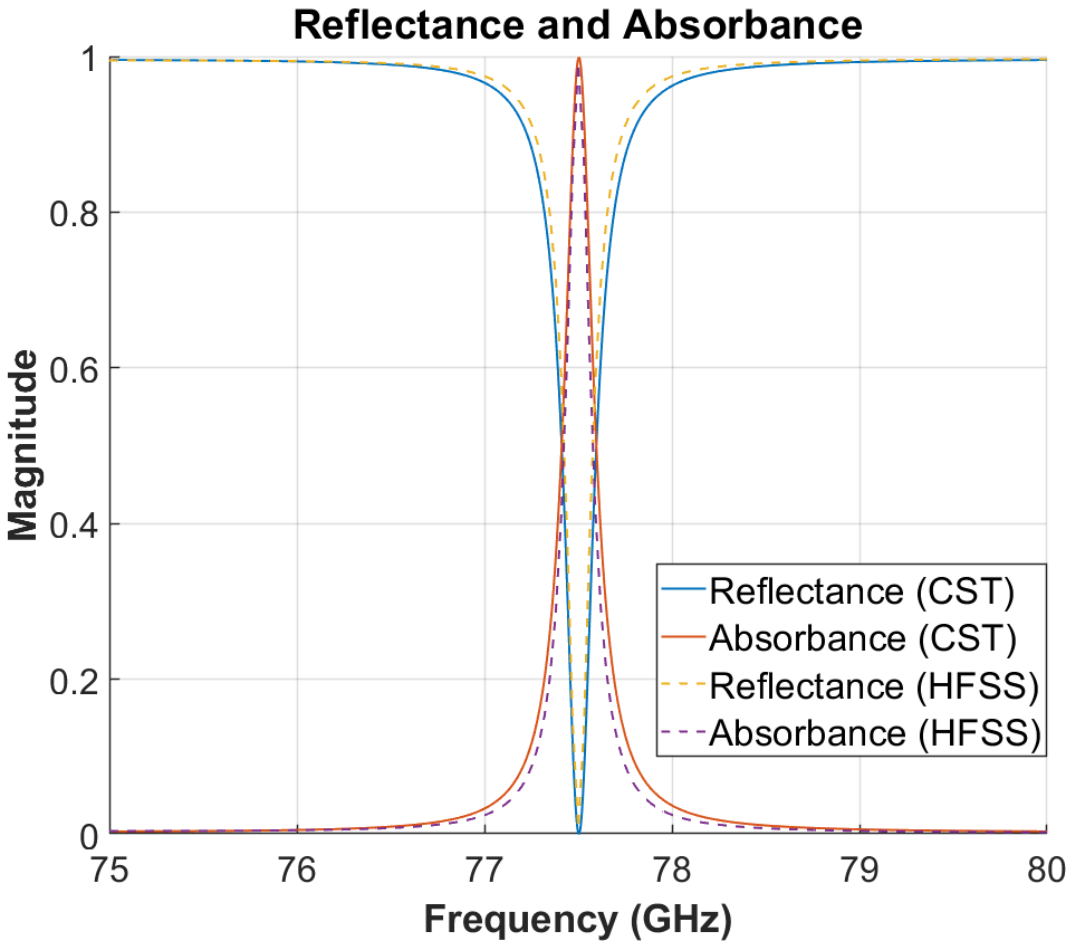


Source: Elaborated by the author.

## 4.5 Formation of Polarization-Independent and Dual-Band Structure

After the individual analysis of the unit cells, a combination using four unit cells was performed, where each cell was rotated by 90 degrees, resulting in a structure with polarization-independent behavior. Furthermore, this configuration exhibited dual-band behavior, maintaining efficiency in both the 77 GHz and 75 GHz ranges with a high-quality factor (Q). Figure 31 illustrates this arrangement, showing the newly designed structure, while Figure 32 provides consistent performance across two frequency bands, which is crucial for various applications.

Figure 31. Arrangement with four unit cells, exhibiting polarization-independent behavior.

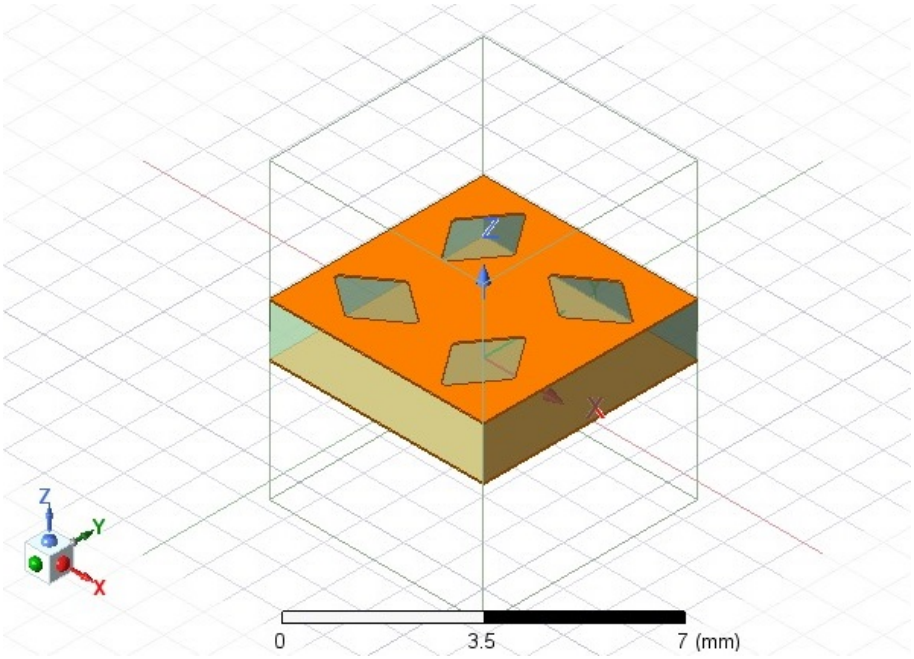


Source: Elaborated by the author.

Figure 32. Result obtained from the Dual Band structure, using the HFSS software.

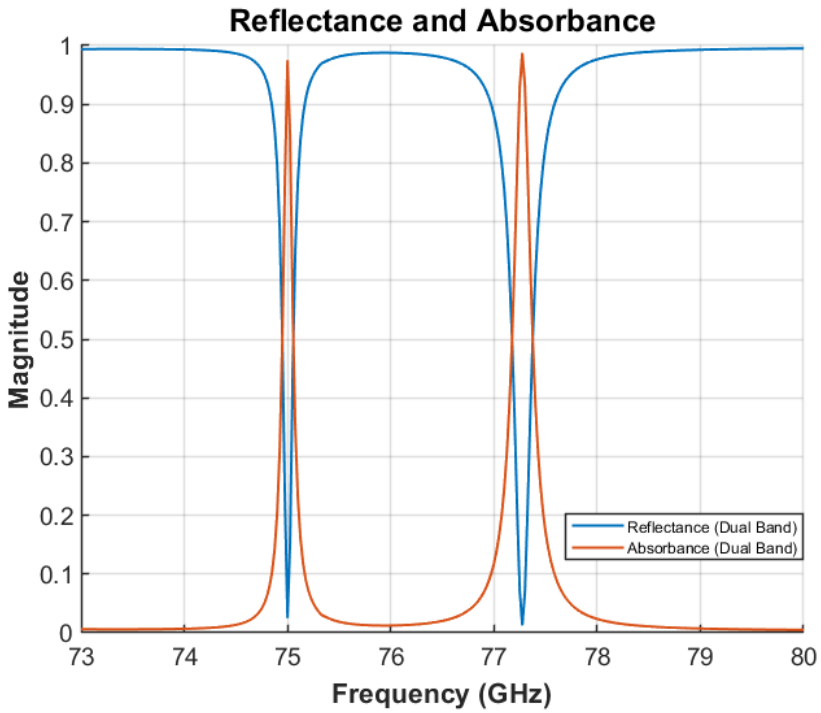


Source: Elaborated by the author.

## 4.6 Comparison Between HFSS, CST, and ANN Results

Figure 33 presents the comparative results between simulations performed in HFSS and CST Studio Suite and the ANN predictions. The central resonant frequency obtained was 77.5 GHz, with an absorption rate of 99.99%, validating the effectiveness of the ANN in optimizing the absorber. The comparison highlights that the ANN was able to replicate traditional results accurately, showcasing the robustness of the proposed approach.

Figure 33. Results obtained using the ANN, comparing HFSS and CST data, with validation provided by the developed Equivalent Circuit Model (ECM-WI).

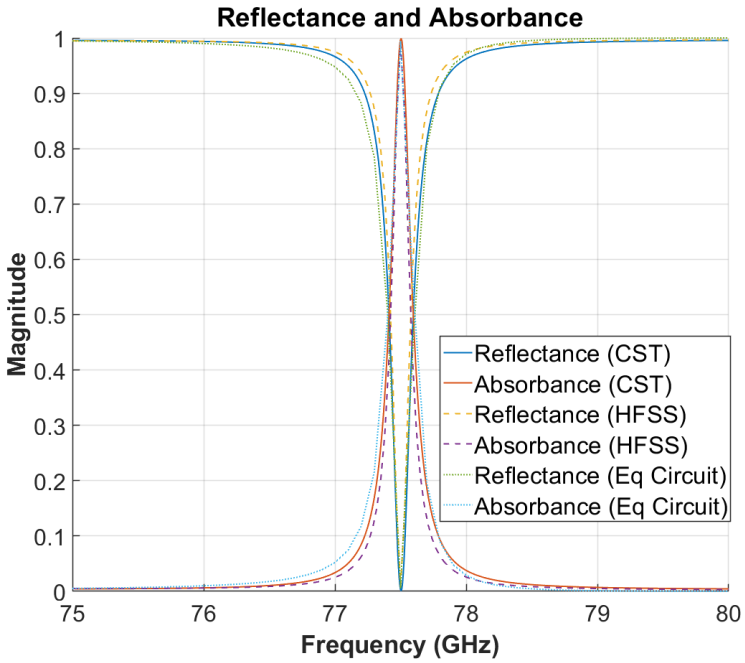


Source: Elaborated by the author.

# 5 Conclusion

This study presents a significant advancement in the optimization of electromagnetic absorbers in the 77 GHz band. The use of Artificial Neural Networks (ANN) as an optimization tool was crucial in achieving a highly efficient absorber with a central resonant frequency of 77.5 GHz and an absorption rate of 99.99%. The ANN allowed for efficient optimization of the absorber's dimensions, considering parameters such as periodicity and diamond dimensions. The combination of the ANN with simulation tools, such as HFSS and CST Studio Suite, demonstrated the accuracy of the approach, providing an optimized design ready for practical applications.

Additionally, the ANN training process highlighted the importance of robust strategies to prevent overfitting. The training halt after 53 epochs was a strategic decision, guided by the monitoring of validation failures. This automatic stopping criterion ensured that the model maintained its generalization capability to unseen data, preventing the network from excessively memorizing the training data and ensuring the robustness of the optimized absorber's parameter predictions.

The addition of an arrangement of four unit cells resulted in a polarization-independent structure capable of operating in two frequency bands (75 GHz and 77 GHz) with a high-quality factor, thereby expanding the absorber's applicability.

To further advance this work, future research should focus on the experimental validation of the optimized absorber's prototype at 77 GHz, alongside investigating its sensitivity to temperature and humidity variations crucial for automotive applications. Additionally, exploring other Artificial Neural Network architectures (e.g., CNNs, RNNs) and multi-objective optimization algorithms could enhance the design process. Finally, developing a more complex and comprehensive equivalent circuit model would refine the theoretical analysis and validate the absorber's performance.

# References


[1] R. Bishop, *Intelligent vehicle technology and trends*, 2005.

[2] Y. Zhang, L.-Y. Zhu, and X.-M. Yang, "Design of dual-band planar thin absorber for vehicular radar test scenario," *International Journal of Electronics*, vol. 111, no. 8, pp. 1319–1330, 2024.

[3] R. Lachner, "Development status of next generation automotive radar in eu," in *ITS Forum, Tokyo*, 2009.

[4] B.-H. Yang and C.-C. Huang, "A 77 ghz planar antenna array in four layer printed circuit board for automotive radar applications," in *2020 15th International Microsystems, Packaging, Assembly and Circuits Technology Conference (IMPACT)*. IEEE, 2020, pp. 45–48.

[5] H. Zheng, L. Chen, and Y. Lee, "High-performance and flexible metamaterial wave absorbers with specific bandwidths for the microwave device," *Crystals*, vol. 13, no. 6, p. 868, 2023.

[6] M. Series, "Systems characteristics of automotive radars operating in the frequency band 76–81 ghz for intelligent transport. systems applications," *Recommendation ITU-R, M*, pp. 2057–1, 2014.

[7] C. Vasanelli, T. Ruess, and C. Waldschmidt, "A 77-ghz cavity antenna array in pcb technology," in *2015 IEEE 15th Mediterranean Microwave Symposium (MMS)*. IEEE, 2015, pp. 1–4.

[8] N. I. Landy, S. Sajuyigbe, J. J. Mock, D. R. Smith, and W. J. Padilla, "Perfect metamaterial absorber," *Physical review letters*, vol. 100, no. 20, p. 207402, 2008.

[9] M. Diem, T. Koschny, and C. M. Soukoulis, "Wide-angle perfect absorber/thermal emitter in the terahertz regime," *Physical Review B—Condensed Matter and Materials Physics*, vol. 79, no. 3, p. 033101, 2009.

[10] Y. Avitzour, Y. A. Urzhumov, and G. Shvets, "Wide-angle infrared absorber based on a negative-index plasmonic metamaterial," *Physical Review B—Condensed Matter and Materials Physics*, vol. 79, no. 4, p. 045131, 2009.

[11] C.-H. Lin, R.-L. Chern, and H.-Y. Lin, "Polarization-independent broad-band nearly perfect absorbers in the visible regime," *Optics express*, vol. 19, no. 2, pp. 415–424, 2011.

[12] C. M. Watts, X. Liu, and W. J. Padilla, "Metamaterial electromagnetic wave absorbers," *Advanced materials*, vol. 24, no. 23, pp. OP98–OP120, 2012.

[13] K. Han, H. B. Shim, and J. W. Hahn, "Optically transparent single-layer frequency-selective surface absorber for dual-band millimeter-wave absorption and low-infrared emissivity," *Advanced Photonics Research*, vol. 4, no. 4, pp. 2 200 009–1–2 200 009–8, 2023.

[14] A. Technologies, "Absorber for automotive radar sensors," http://www.arc-tech.com, 2024, accessed: Aug. 17, 2024.

[15] E. . Cuming, "Microwave absorbers for high frequencies used in automotive applications," http://www.eccosorb.eu, 2024, accessed: Aug. 17, 2024.

[16] R. Imanirad, X.-S. Yang, and J. S. Yeomans, "Stochastic decision-making in waste management using a firefly algorithm-driven simulation-optimization approach for generating alternatives," in *Simulation-Driven Modeling and Optimization: ASDOM, Reykjavik, August 2014*. Springer, 2016, pp. 299–323.

[17] M. A. Neto, J. Araújo, F. Barros, A. Silva, G. Cavalcante, and A. d'Assunção, "Bioinspired multiobjective synthesis of x-band fss via general regression neural network and cuckoo search algorithm," *Microwave and Optical Technology Letters*, vol. 57, no. 10, pp. 2400–2405, 2015.

[18] M. A. Neto, F. Barros, J. Araújo, H. Gomes, G. Cavalcante, and A. D'Assunção, "A metaheuristic hybrid optimization technique for designing broadband fss," in *2015 SBMO/IEEE MTT-S International Microwave and Optoelectronics Conference (IMOC)*. IEEE, 2015, pp. 1–5.

[19] M. C. Neto, J. P. Araújo, R. J. Mota, F. J. Barros, F. H. Ferreira, G. P. Cavalcante, and B. S. Castro, "Design and synthesis of an ultra wide band fss for mm-wave application via general regression neural network and multiobjective bat algorithm," *Journal of Microwaves, Optoelectronics and Electromagnetic Applications*, vol. 18, no. 4, pp. 530–544, 2019.

[20] R. Mittra, "Techniques for analyzing frequency selective surfaces-a review," *Proc. IEEE*, vol. 76, no. 12, pp. 1539–1614, 1998.

[21] L. C. M. d. Moura, "Caracterização de fss com geometria estrela de quatro braços tipo fenda," Master's thesis, 2016.

[22] J. d. N. Cruz, "Caracterização de fss com geometria matrioska aberta," Master's thesis, 2014.

[23] Y. Xu, R. Sui, J. Wang, and D. Feng, "Time-varying reflectivity modulation on inverse synthetic aperture radar image using active frequency selective surface," *Electronics*, vol. 11, no. 20, p. 3318, 2022.

[24] F. Hopkinson and D. Rittenhouse, "An optical problem, proposed by mr. hopkinson, and solved by mr. rittenhouse," *Transactions of the American Philosophical Society*, vol. 2, pp. 201–206, 1786.

[25] A. S. Maia, "Projeto de absorvedores de micro-ondas do tipo banda dupla usando superfícies seletivas em frequência," 2022.

[26] B. A. Munk, *Frequency selective surfaces: theory and design*. John Wiley & Sons, 2005.

[27] C. da Cruz Nogueira, "Aplicação do cst no estudo de fss de ferrite magnetizada para filtragem de ondas eletromagnéticas em sistemas de radar veicular inteligente," Belém, PA, Brasil, jul 2019.

[28] V. H. B. de Magalhães, "Aplicação da ferramenta de análise numérica cst e estudo parametrizado de ferramentas bioinspiradas aplicadas à otimização de fss," 2017, monografia, Universidade Federal do Pará, Brasil.

[29] A. L. P. d. S. Campos, "Superfícies seletivas em frequência: análise e projeto," 2008.

[30] J. C. Vardaxoglou, "Frequency selective surfaces: analysis and design," *(No Title)*, 1997.

[31] T. R. de Sousa, "Desenvolvimento de superfícies seletivas em frequência baseadas na geometria matrioska independente da polarização," *João Pessoa, Paraíba: Instituto Federal da Paraíba, PPGEE, Dissertação de Mestrado*, 2019.

[32] S. Narayan, K. Prasad, R. Nair, and R. Jha, "A novel em analysis of cascaded thick fss using mode-matching generalized scattering matrix technique," in *2011 IEEE Applied Electromagnetics Conference (AEMC)*. IEEE, 2011, pp. 1–4.

[33] D. Webb, E. Michielssen, and R. Mittra, "Thick frequency selective surfaces," in *IEEE Antennas and Propagation Society International Symposium 1992 Digest*. IEEE, 1992, pp. 1795–1798.

[34] P. Harms, R. Mittra, and W. Ko, "Implementation of the periodic boundary condition in the finite-difference time-domain algorithm for fss structures," *IEEE Transactions on Antennas and Propagation*, vol. 42, no. 9, pp. 1317–1324, 1994.

[35] B. Sanz-Izquierdo and E. Parker, "Dual polarized reconfigurable frequency selective surfaces," *IEEE Transactions on Antennas and Propagation*, vol. 62, no. 2, pp. 764–771, 2013.

[36] G. I. Kiani, "Passive, active and absorbing frequency selective surfaces for wireless communication applications," Ph.D. dissertation, Macquarie University, 2009.

[37] T. R. Sousa, "Desenvolvimento de superfície seletiva em frequência baseada na geometria matrioska independente da polarização," Master's thesis, 2019.

[38] S.-D. Jang, B.-W. Kang, and J. Kim, "Frequency selective surface based passive wireless sensor for structural health monitoring," *Smart Materials and Structures*, vol. 22, no. 2, p. 025002, 2012.

[39] L. C. M. d. M. Fontoura, "Novo método de síntese de fss multibanda baseado em aprendizado de máquina para sistemas de comunicação sem fio," 2021.

[40] J. T. Murugan, T. S. Kumar, P. Salil, and C. Venkatesh, "Dual frequency selective transparent front doors for microwave oven with different opening areas," *progress in electromagnetics research letters*, vol. 52, pp. 11–16, 2015.

[41] T. Wu, "Frequency selective surface and grid array (a wiley interscience publication)," 1995.

[42] R. H. C. Maniçoba, "Estudo do acoplamento entre superfícies seletivas de frequência assimétricas em estruturas de multicamadas," 2012.

[43] A. Campos, A. Assunção, and M. Melo, "Aplicação de superfícies seletivas em frequência em radomes dielétricas para antenas de microondas," in *XIX Simpósio Brasileiro de Telecomunicações*, 2001.

[44] R. Saidi, M. Titaouine, A. Djouimaa, I. Adoui, K. Bencherif, T. R. De Sousa, A. G. Neto, and H. Baudrand, "Analysis and synthesis of multiband dual polarized parallel metallic strips fss with a ring using wcip method," *AEU-International Journal of Electronics and Communications*, vol. 96, pp. 294–302, 2018.

[45] Z. N. Chen, X. Qing, Y. P. Zhang, Z. Shen, E. L. Tan, and E. P. Li, "Antenna research and development in singapore," in *2013 7th European Conference on Antennas and Propagation (EuCAP)*. IEEE, 2013, pp. 161–165.

[46] Y. Rahmat-Samii and A. N. Tulintseff, "Diffraction analysis of frequency selective reflector antennas," *IEEE transactions on antennas and propagation*, vol. 41, no. 4, pp. 476–487, 1993.

[47] A. G. Neto, J. Silva, J. Souza, M. Alencar, and T. Evangelista, "Desenvolvimento de uma fss banda dupla para aplicações em paredes inteligentes," *XXXV Simpósio Brasileiro de Telecomunicações e Processamento de Sinais*, pp. 67–71, 2017.

[48] P. Neto, A. L. P. Campos, and A. G. Neto, "Frequency selective surface microwave absorber for wlan applications," *Journal of Communication and Information Systems*, vol. 35, no. 1, p. 208, 2020.

[49] D. Kundu, A. Mohan, and A. Chakrabarty, "Single-layer wideband microwave absorber using array of crossed dipoles," *IEEE Antennas and Wireless Propagation Letters*, vol. 15, pp. 1589–1592, 2016.

[50] E. L. Nohara, "Materiais absorvedores de radiação eletromagnética (8-12 ghz) obtidos pela combinação de compósitos avançados dielétricos e revestimentos magnéticos." 2003.

[51] I. Choi, D. Lee *et al.*, "Optimum design method of a nano-composite radar absorbing structure considering dielectric properties in the x-band frequency range," *Composite Structures*, vol. 119, pp. 218–226, 2015.

[52] J. F. Shaeffer and M. T. Tuley, *Radar cross section: its prediction, measurement and reduction.* Artech House, 1985.

[53] R. S. Anwar, L. Mao, and H. Ning, "Frequency selective surfaces: A review," *Applied Sciences*, vol. 8, no. 9, p. 1689, 2018.

[54] T. Weiland, "Finite integration method and discrete electromagnetism," in *Computational Electromagnetics: Proceedings of the GAMM Workshop on Computational Electromagnetics, Kiel, Germany, January 26–28, 2001.* Springer, 2003, pp. 183–198.

[55] M. Clemens and T. Weiland, "Discrete electromagnetism with the finite integration technique," *Progress In Electromagnetics Research*, vol. 32, no. 32, pp. 65–87, 2001.

[56] J. Silvestro, "Hybrid finite element boundary integral method," *Ansys, Inc.[online]. Available: https://support. ansys. com*, 2010.

[57] R. Corporation, "Rt/duroid 5880 laminates," https://www.rogerscorp.com/advanced-electronics-solutions/rt-duroid-laminates/rt-duroid-5880-laminates, 2024.

[58] A. Forsyth, "Review of resonant techniques in power electronic systems," *Power Engineering Journal*, vol. 10, no. 3, pp. 110–120, 1996.

[59] G. S. Kumar and K. Rajasekhar, "Performance analysis of levenberg-marquardt and steepest descent algorithms based ann to predict compressive strength of sifcon using manufactured sand," *Engineering science and technology, an international journal*, vol. 20, no. 4, pp. 1396–1405, 2017.

[60] D. Z. Huang, K. Xu, C. Farhat, and E. Darve, "Learning constitutive relations from indirect observations using deep neural networks," *Journal of Computational Physics*, vol. 416, p. 109491, 2020.

[61] F. C. Seman and N. K. Khalid, "Design strategy for optimum planar square loop fss with different dielectric substrates," in *Theory and Applications of Applied Electromagnetics: APPEIC 2014*. Springer, 2015, pp. 87–94.